TECHNICAL MEMO

ITASCA

Date: July 9, 2026

To: PFC Documentation Set

From: David Potyondy

Re: SNBV Support (Subspring Network Breakable Voronoi model) for PFC [snbvPkg9.5]

Ref: 5-8106:25TM06

This memo describes support for using the Subspring Network Breakable Voronoi model that includes material creation and laboratory testing (direct-tension and triaxial/biaxial in 3D/2D). The capability is provided in the **`snbvPkg9.N`** package that works with PFC2D/3D version 9 (where **`N`** is the package subversion number). The SNBV model is a type of bonded-particle model and support for constructing other types of bonded-particle models is provided by the material modeling support package (Potyondy, 2025).

TABLE OF CONTENTS

1.0 SUBSPRING NETWORK BREAKABLE VORONOI MODEL

The Subspring Network contact model with rigid, Breakable, Voronoi-shaped grains is called the SNBV model (Potyondy et al., 2025) and is provided in PFC2D and PFC3D (ITASCA, 2026). The definitive definition of the model is given in Potyondy et al. (2025). The model was developed as part of the work described in the Potyondy et al. (2024) report. The two papers Potyondy and Fu (2024) and Potyondy and Purvance (2024) provide a summary of what is in the report. The SNBV model mimics the microstructure of a granite (see Figure 1).

Figure 1 Microstructure of granite and SNBV model.

The model is summarized in the following abstract of Potyondy et al. (2025).

> A microstructural rock model based on the distinct element method employing the Subspring Network contact model with rigid, Breakable, Voronoi-shaped grains (SNBV model) is proposed. The model consists of a mesh (3D Voronoi tessellation) of rigid, breakable, Voronoi blocks. The SNBV model is a microstructural rock model because it is a discrete model that can mimic rock microstructure at the grain scale. SNBV material mimics the microstructure of angular, interlocked, breakable grains with interfaces that may have an initial gap and can sustain partial damage. The model embodies the microstructural features and damage mechanisms that occur at the grain scale: initial microcrack fabric; heterogeneity-induced local tension; and intergranular and transgranular damage. The heterogeneity-induced local tension can be introduced in a controlled fashion that is not tied directly to the shape and packing of the grains and the interface stiffnesses. The synthetic material exhibits behavior during direct-tension and triaxial compression tests that matches the behavior of compact rock. The material can be calibrated to match the standard material properties and characteristic stresses of pink Lac du Bonnet granite. The material properties consist of Young's modulus and Poisson's ratio corresponding with uniaxial compression and Young's modulus corresponding with direct tension, as well as tensile strength, crack-closure stress, crack-initiation stress, secondary crack-initiation stress to mark the onset of grain breakage, crack-damage stress, and compressive strengths up to 4 MPa

confinement. The model is suitable for studying the grain-scale micromechanics of brittle rock fracture.

1.1 Sanctioning the Model

A conceptual framework for sanctioning (or gaining confidence in) a microstructural model is outlined in Potyondy (2015) and summarized as follows. No model is complete or fully verifiable (Oreskes et al., 1994); instead, the best that can be done is to sanction the model. According to Winsberg (2010, p. 23):

> The sanctioning of simulations does not cleanly divide into verification and validation. In fact, simulation results are sanctioned all at once: simulationists try to maximize fidelity to theory, to mathematical rigor, to physical intuition, and to known empirical results. But it is the *simultaneous confluence* of these efforts, rather than the establishment of each one separately, that ultimately gives us confidence in the results.

The SNBV model is a type of bonded-particle model (BPM, as defined in Potyondy et al. [2025]). BPMs of intact rock have been sanctioned by demonstrating that they match the response obtained during direct-tension and compression tests of a typical compact rock. This response consists of the properties measured during such tests as well as the microstructural behavior that occurs during such tests. The microstructural behavior is viewed through the lens of the interpretive framework illustrated in Figure 2, which allows one to relate the model behavior to that of the rock. In some cases, the BPM parameters are chosen to approximate the true microstructural properties, and then the macroscopic behavior is studied. But in most cases, either the true microstructural properties are not known, or the BPM is a simplification of the true microstructural features. In such cases, the BPM parameters must be chosen by performing a calibration process in which a particular instance of a BPM is used to simulate a set of material tests, and the BPM parameters are chosen to reproduce the relevant response occurring in such tests. In addition to the laboratory-scale tests noted above, field-scale tests that may include excavation-induced damage have also been used in the sanctioning process.

The SNBV model is sanctioned at the grain scale by a calibration process in which a particular instance of the model is used to simulate direct-tension and triaxial compression tests to reproduce the relevant macroscopic properties and microstructural behavior (see Figure 2).

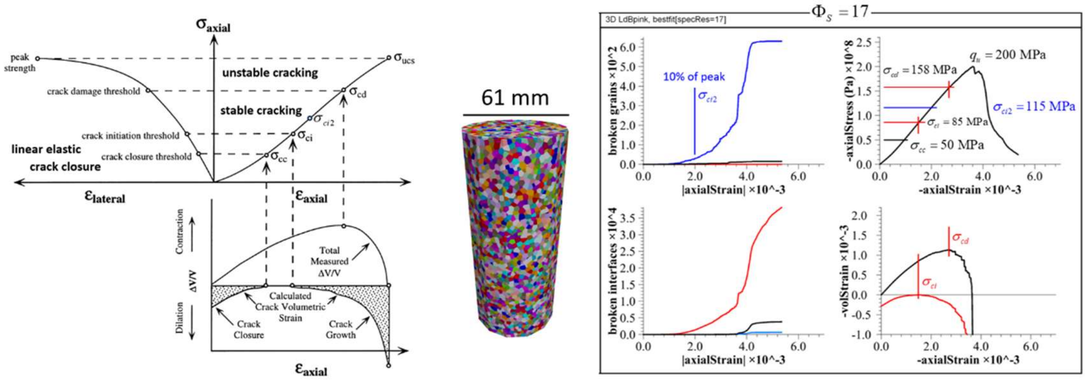

Stress-strain curves from uniaxial compression test on compact rock showing the stages in its progressive failure.

Stress-strain curves from uniaxial compression test on SNBV model of pink Lac du Bonnet granite.

Figure 2 Sanctioning of SNBV model.

1.2 Essential Features

The SNBV model combines the subspring network contact model at the interfaces between Voronoi blocks with gap initialization and grain breakage. The essential features of these two components are summarized here.

The essential features of the subspring network contact model are as follows (see Figure 3). Each contact is between two polygonal surfaces. The interface is modeled as a disk with the same area as that of the polygon. There are three subcontacts arranged symmetrically around the edge of the disk. Each subcontact behaves like a simplified spring network contact model, carries both force and moment, and can be in a bonded or unbonded state. The bond breaks when either the tensile or shear strength is exceeded, and the subcontact then exhibits frictional behavior. There can be partial damage at a contact when less than three of the subcontacts have broken. The fictitious-force contribution is only applied to a bonded subcontact. The interface of the 2D model is a line of the same length as the polygonal edge, with a subcontact at each end.

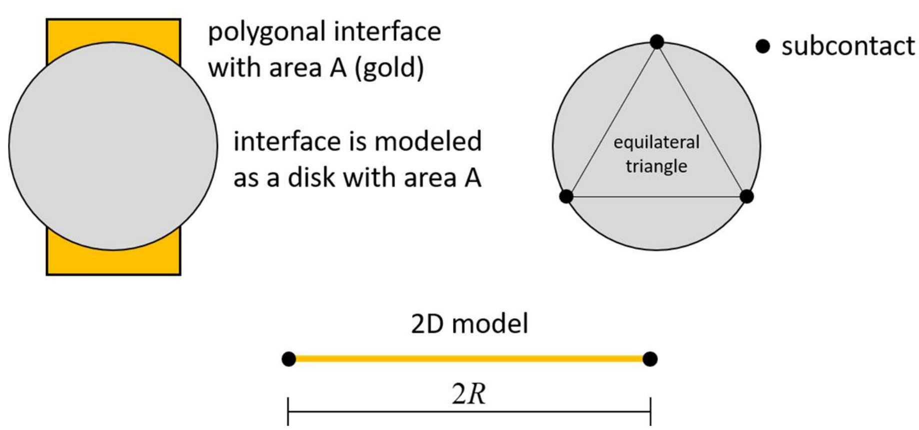

Figure 3 Interface between Voronoi cells in the subspring network contact model. The interface is modeled as a disk with three subcontacts in the 3D model, and as a line with a subcontact at each end in the 2D model.

The Rigid Body Spring Network (RBSN) lattice scheme of Bolander and Sato (1998) provides a direct method to compute interface stiffnesses based on the Voronoi cell geometries, resulting in a homogenous elastic response at the grain scale. In the RBSN scheme, there is a single contact at the centroid of each interface. The six spring stiffnesses are a function of the specified contact modulus and the geometric arrangement of the two contacting surfaces as shown in Figure 4 and defined by contact modulus $\left(E_c\right)$; interface area $\left(A_{ij}\right)$; distance between seed positions of the Voronoi cells $\left(h_{ij}\right)$; and polar and two principal moments of inertia of the interface polygon (J, I_s, and I_t). If the same contact modulus is assigned to all contacts in the model, then there will be a linear elastic isotropic material response with a macroscopic Young's modulus equal to the contact modulus and a macroscopic Poisson's ratio of zero. A non-zero Poisson's ratio is obtained via a fictitious-force correction (Asahina et al., 2015, 2017) that applies fictitious forces to each Voronoi cell. When the fictitious-force correction is applied, if the same contact modulus is assigned to all contacts in the model, and the same contact Poisson's ratio is assigned to all contacts in the model, then there will be a linear elastic isotropic material response with a macroscopic Young's modulus equal to the contact modulus and a macroscopic Poisson's ratio equal to the contact Poisson's ratio. In addition, there will be negligible tensile forces generated if the material is uniaxially compressed.

The 3D subspring network contact model differs from the RBSN scheme as follows. There are three subcontacts at each interface. The six stiffnesses at each subcontact are set equal to one third of those shown in Figure 4 with the h_{ij} terms taken as the centroid positions of the Voronoi cells.[1] The 2D Subspring Network scheme has two subcontacts at each interface. The three

[1] This modification appears to introduce some grain scale elastic heterogeneity into the model. Further study is warranted and is underway, and the study results will be added to this memo. Rasmussen (2026) provides the following relevant information. {In the manuscript it is stated: "Because the SNBV cohesion and friction angle are interface-scale input parameters, they were not assumed to be automatically identical to the macroscopic Mohr–Coulomb parameters." // From Bolander and my previous works, including the 2019 and 2024 ones, it was shown that the macroscopic cohesion and friction angle are exactly equal to the interface parameters. The procedure suggested is the one that I adopted in my 2024 paper related to the Mine-by tunnel, which was an interesting procedure due to its practicality and accurate back-analysis of the HDZ. The reason interface parameters and macroscale ones are a little different in PFC is because the distance between the centroids are being used to calculate the springs' stiffness in the PFC formulation. However, the correct distance considering the RBSN formulation is the nucleis' distance. This makes a huge difference. For example, my failure mode in the mine-by tunnel was clearer and more well-defined exactly because of this. // Please, this should be somehow clarified in the manuscript, that Bolander RBSN, Rasmussen (2024) and Hybrid LDEM previously used the distance between nuclei to calculate the springs stiffness, while in PFC the distance between the centroids are used. In PFC, this brings additional spurious stress heterogeneity and a difference between the interface and macroscale properties that grows larger as the difference in Voronoi cell sizes grows bigger in the model. But it is not because "cohesion and friction angle are interface-scale input parameters". This explanation is not the correct reason why interface parameters and macroscale ones (considering the intact material prior to rupture) are not 100% perfectly matched to machine precision.}

stiffnesses at each subcontact are set equal to one half of these shown in Figure 4 with the h_{ij} terms taken as the centroid positions of the Voronoi cells and

$$\begin{gathered} k_t = k_{\phi n} = k_{\phi t} = 0 \\ A_{ij} = 2Rt, \quad I_s = \frac{2R^3 t}{3}, \quad t = 1 \end{gathered} \tag{1}$$

where $2R$ is the interface length (see Figure 3).

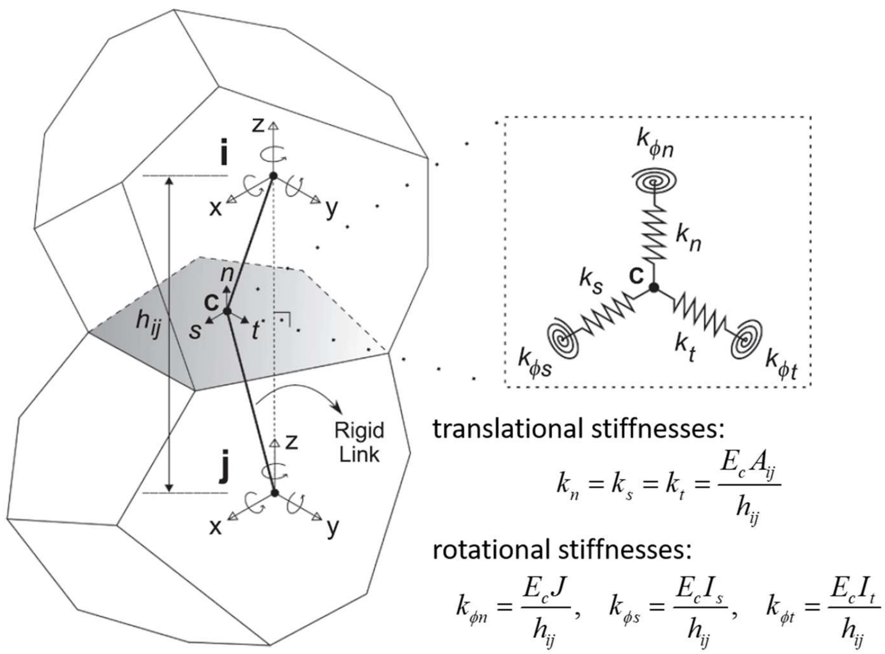

Figure 4 ***Interface between Voronoi cells in the RBSN scheme and assignment of six stiffnesses.*** (From Fig. 2 of Rasmussen [2021]

The SNBV model provides grain breakage with a replaceable-particle scheme that uses a stress-based failure criterion, together with a Weibull distribution of strengths, and a size effect on strength, to determine whether a grain (modeled as a PFC rigid block) will break. The grain is assumed to behave like a laboratory-scale rock specimen with strength given by the Hoek–Brown failure criterion for compressive failure and a tension cut-off for tensile failure. Damage that forms during compressive failure of compact rock consists of axial splitting under low confinement, and shear-band formation under high confinement. The SNBV model is suited for low-confinement conditions, and thus, a shear-band failure mode is not provided.[2] When the strength is exceeded, then the polyhedral grain is split into two smaller polyhedra. The split occurs on a plane through

[2] Rasmussen (2022) provided the shear-band failure mode by splitting the grain along a plane oriented 45 degrees with respect to the maximum and minimum principal stress directions with a 50% probability of occurring in either the clockwise or counter-clockwise direction.

the grain centroid and oriented perpendicular to the least compressive principal stress direction. If the split operation would produce a sliver, then the grain is not cut.[3]

1.3 Material Creation

The SNBV material consists of grains and interfaces. The material-creation process involves (1) generating the grains and trimming them to conform to the specimen shape, and (2) creating the interfaces and assigning properties to both grains and interfaces.[4]

1.3.1 Grain Structure Generation

The grain structure is produced by generating grains and trimming them to conform to the specimen shape.[5] The grain structure is a mesh of perfectly interlocking polyhedral blocks generated as follows (see Figures 5 and 6). A collection of non-overlapping spheres[6] with a uniform size distribution is generated with the **ball generate** command in a region that is larger than the region that will contain the final cylindrical specimen. The generation process places a trial sphere at a random location in the region and keeps that sphere only if it does not overlap an existing sphere, with the process continuing until no further non-overlapping spheres can be inserted. This generation process ensures that the spheres are packed as closely as possible without overlapping. The spheres are used as seeds for a conformal Voronoi tessellation generated by the **rblock construct from-balls polydisperse true** command to produce a Laguerre tessellation that uses the sphere diameters to weight the cell boundaries so that the cell sizes follow the sphere size distribution. The spheres are deleted and each Voronoi cell defines a PFC rigid block (or grain). Equal-diameter spheres are used in Potyondy et al. (2025) to provide a simple material. If the initial spheres are drawn from a uniform size distribution with a maximum to minimum diameter ratio of five, then the width of the grain size distribution is increased (see Figure 7). Further study is warranted to determine the effect of grain size distribution on material response.

The collection of grains is then trimmed to form a cylindrical or rectangular shape with the **rblock cut sliver-remove false** command. The trimming process splits grains that cross the cylinder or rectangle boundary thereby producing polyhedra that remain convex but are no longer Voronoi

---

[3] The cut produces a sliver if the ratio (V_c/V_o) is less than 0.05, where V_c is the smallest volume of the two potential polyhedra and V_o is the volume of the original polyhedron.

[4] {DP: The imperfect match of micro and macro Young's modulus and Poisson's ratio for the present models may be caused by assigning the interface properties after trimming the grains because the positions of the particle centroids used to compute the $\left(h_{ij}\right)$ in Figure 4 differ greatly from their positions before trimming. This hypothesis will be investigated.}

[5] The grain-generation properties are specified in file **`makeGrains.dat`**. The specimen and grain-size distribution are provided in plots **`specimen`** and **`propGrains`**, respectively.

[6] The 2D model uses the procedure described here, except that the operations are performed upon disks instead of spheres.

cells.[7] There are numerous small grains near the surface; however, they have a minor effect of the grain size distribution as shown in Figure 8. Specimen resolution is the average number of grains of virgin material (material before trimming) across the specimen diameter

$$\Phi_S = \frac{D}{d_{50}} \tag{2}$$

where D is specimen diameter and d_{50} is average grain size of the virgin material. Specimen resolution is used to define a representative volume.[8]

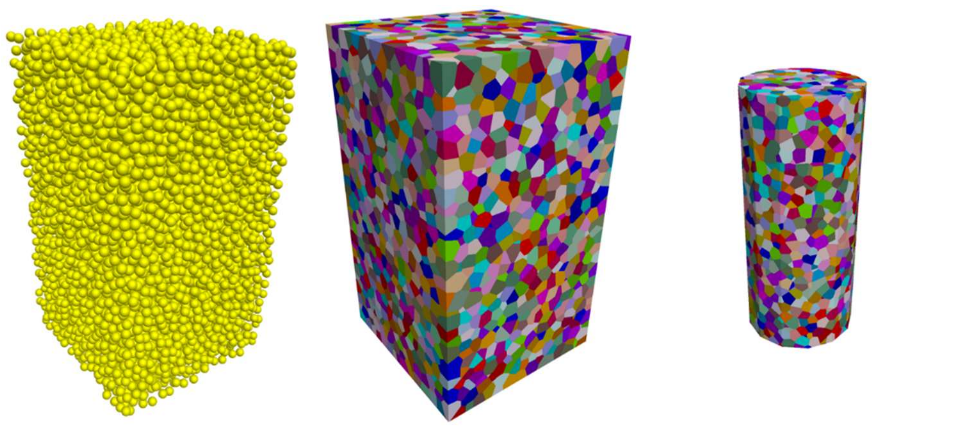

Figure 5 Grain-structure generation (3D model).

[7] Trimming may be important because meshing to boundaries may produce "keystone" effects, whereby the specimen is strengthened because of mesh regularity at the boundaries. The model of Rasmussen (2022) is like the SNBV model, but it does not exhibit keystone effects. Further study is warranted to determine why this is.

[8] Potyondy et al. (2025) found that the same mechanical response was obtained for 3D specimen resolutions of 9 and 17 such that a specimen resolution of nine defined a representative volume.

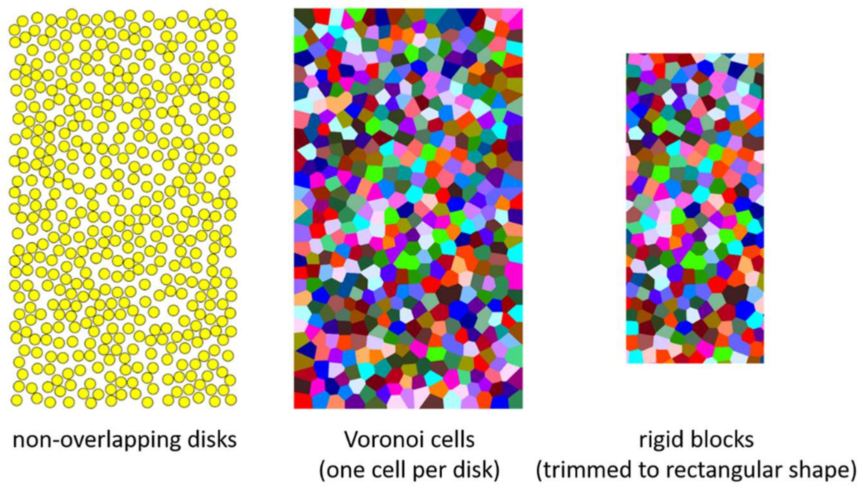

Figure 6 Grain-structure generation (2D model).

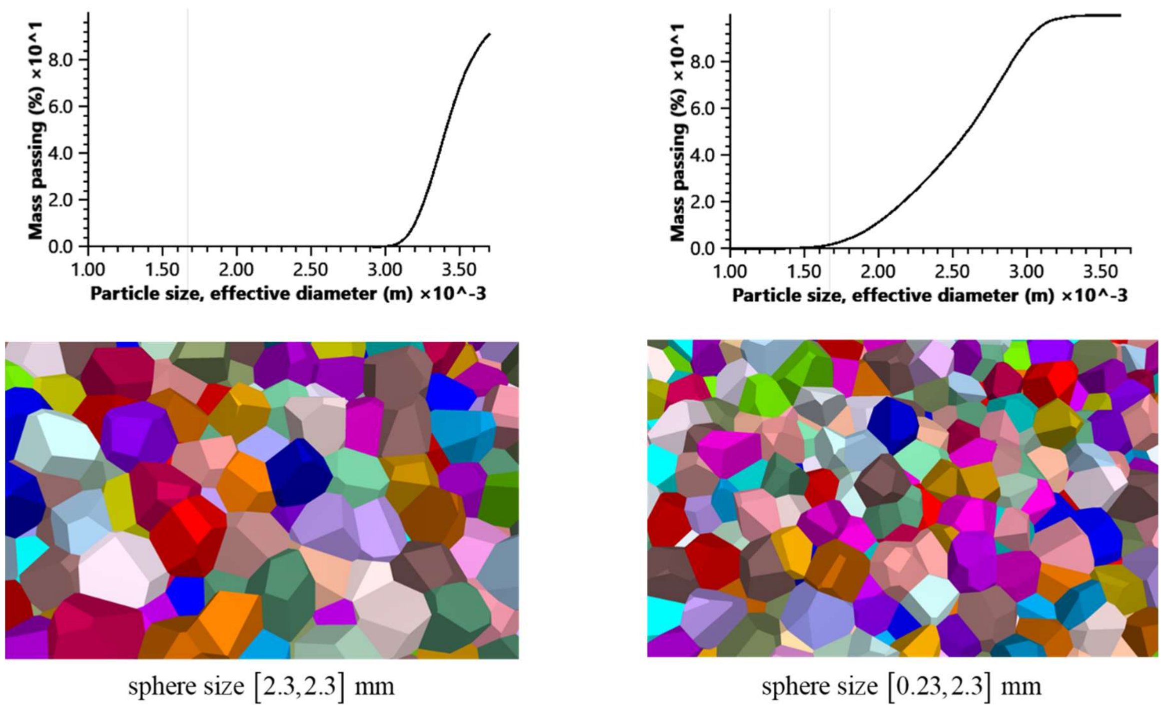

Figure 7 Effect of sphere size distribution on 3D grain structure, showing grain size distributions and grains within the material.

$$\Phi_S = 17$$

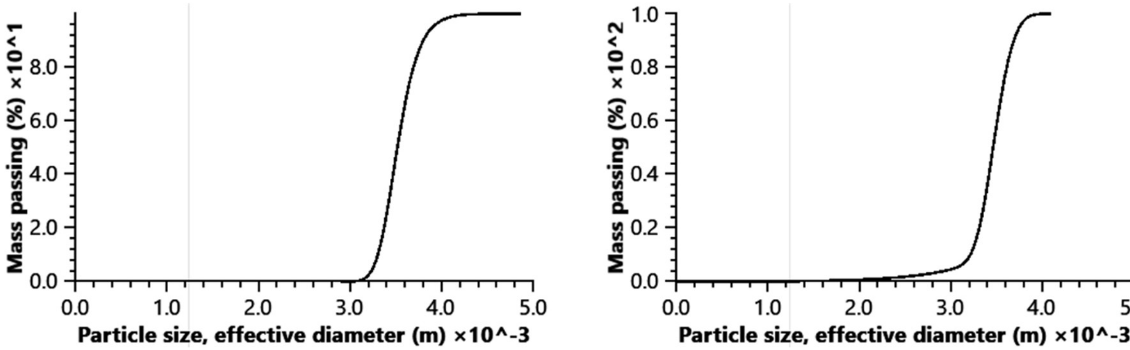

Figure 8 Grain size distributions before and after carving a specimen out of the initial block of material.

1.3.2 Material Property Assignment

Given the perfectly interlocked grains, interfaces are created, and properties are assigned to both grains and interfaces.[9] The grains are dilated by a small amount with the **rblock dilate** command. Interfaces are created at the overlapping polygonal facets with the **model clean** command. Properties (defined in Table 1) are assigned to both grains and interfaces. There are four sets of material parameters: deformability, microcrack fabric, interface strength, and grain strength. The Weibull distribution is a continuous probability distribution that can fit an extensive range of distribution shapes. The Weibull distribution (see Section 2.1) is used to introduce material heterogeneity into the model (via the deformability, microcrack fabric, and strength properties) and to characterize the size effect on grain strength. A Weibull distribution is defined by mean value $(\bar{x})$ and shape factor (m).[10] The strength and non-strength parameters that satisfy a Weibull distribution use the terms Weibull modulus and shape factor, respectively, for the m parameter.

[9] Material properties are specified in file **`makeMaterial.dat`**. Probability density histograms of interface tensile strength, contact modulus, and microcrack fabric gap as well as cumulative distribution function of microcrack fabric gaps-and-slits are provided in plot **`propContacts`**.

[10] The mean value and shape factor are related to the Weibull characteristic value of Eq. (13) via Eq. (15).

Table 1 SNBV Material Parameters

Symbol [FISH]	Name
Deformability	
$\bar{E}_c$ `[young]`	contact modulus (mean)
m_E `[mE]`	Weibull shape factor for contact modulus [1]
ν_c `[pois]`	contact Poisson's ratio
Microcrack Fabric	
$\{\varphi_B, \varphi_G\}$ `[phiB, pfhiG]`	bonded and gapped fractions, slit fraction $(\varphi_S = 1 - \varphi_B - \varphi_G)$
$\bar{g}$ `[gap]`	gap size (mean)
m_G `[mG]`	Weibull shape factor for gap size [1]
Interface Strength	
$\bar{\sigma}_t$ `[test]`	tensile strength (mean)
m_S `[mS]`	Weibull modulus for tensile strength [1]
γ `[cohRat]`	cohesion to tensile strength ratio (c/σ_t)
ϕ `[fa]`	friction angle $(\tau_c = c + \sigma \tan(\phi))$
ϕ_r `[faRes]`	residual friction angle $(\mu = \tan(\phi_r))$
Grain Strength	
d_r `[dr]`	size (effective diameter) of reference grain
$\bar{\sigma}_T^r$ `[tenStrG]`	tensile strength of reference grain (mean)
m_{SG} `[mSG]`	Weibull modulus for reference grain tensile strength [1]
γ_g `[UCSrat]`	UCS to tensile strength ratio (σ_c/σ_T) [2]
m_i `[m_i]`	Hoek-Brown material constant
m_{SE} `[mSE]`	Weibull modulus for size effect on grain tensile strength

[1] Setting this value to 10,000 gives homogeneous values.

[2] This is the correct ratio. The ratio given in Table 1 of Potyondy et al. (2025) is incorrect.

The **deformability parameters** assign contact modulus and contact Poisson's ratio (ν_c) to the interface at each contact using the **compute-stiffness** method. The values are assigned to all subcontacts. The contact moduli satisfy a Weibull distribution with mean $\bar{E}_c$ and Weibull shape factor m_E. The contact Poisson's ratios are the same at all contacts. The contact modulus and contact Poisson's ratio of new interfaces that may form after material creation are set to $\bar{E}_c$ and ν_c, respectively.

The **microcrack-fabric parameters** assign each contact to be either bonded, gapped, or slit based on the number fractions of the bonded and gapped types (see Figure 9). The number fractions are defined as

$$\begin{gathered} \varphi_B = n_B / n_c, \quad \varphi_G = n_G / n_c, \quad \varphi_S = n_S / n_c \\ n_c = n_B + n_G + n_S, \quad \varphi_B + \varphi_G + \varphi_S = 1 \end{gathered} \tag{3}$$

where φ_B, φ_G, and φ_S are bonded, gapped, and slit fractions, respectively; n_B, n_G, and n_S are the number of bonded, gapped, and slit contacts, respectively; and n_c is the total number of contacts. Fabric types are assigned randomly to each contact. The gapped contacts are assigned gap values that satisfy a Weibull distribution. The slit and bonded contacts are assigned a gap of zero. The contacts are bonded using the **bond** method, and the contact gaps are installed by setting the reference-gap property equal to the negative of the desired gap. The bond state and gap of the contact is assigned to each subcontact; thus, a bonded contact has all subcontacts in the bonded state.

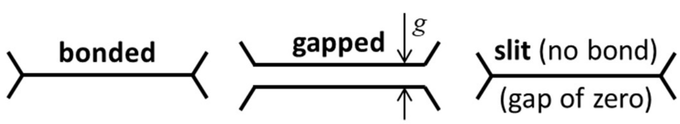

Figure 9 ***Microcrack fabric consisting of bonded, gapped, and slit contacts. The bonded and slit contacts have coincident surfaces, while the gapped contacts have a uniform, non-zero gap between the surfaces (i.e., all subcontacts have the same gap).***

The microcrack fabric that can be created is illustrated with the following example. Consider a material that has 20% of its contacts bonded, and 60% of its contacts gapped; therefore, the remaining 20% of its contacts are slits. The gapped contacts are assigned gap values that satisfy a Weibull distribution with a mean gap size of 1×10^{-5} m, and a Weibull shape factor of 5.0. The probability density for the gapped contacts and cumulative distribution functions for the gapped and slit contacts are shown in Figure 10.

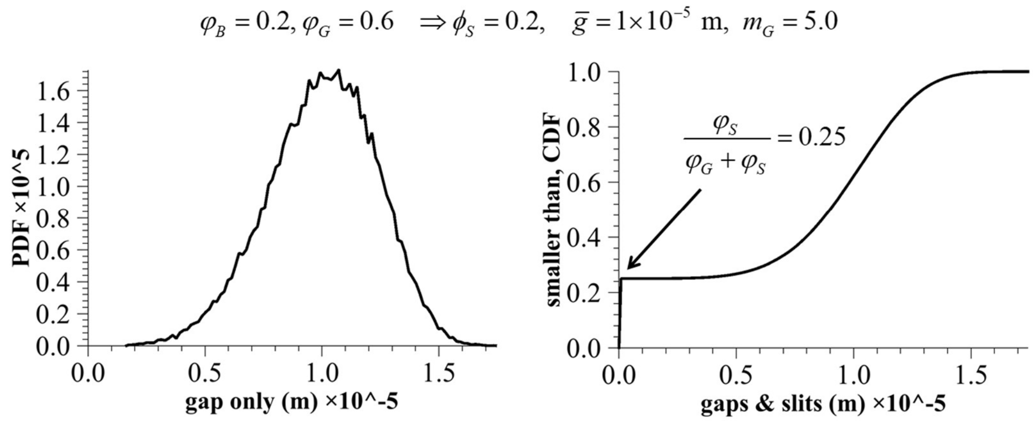

Figure 10 Probability density (left) and cumulative distribution (right) functions for the example microcrack fabric.

The **interface-strength parameters** assign tensile strength (σ_t), cohesion (c), friction angle (ϕ) , and residual friction angle (ϕ_r) to the interface at each contact. The values are assigned to all subcontacts. New interfaces that may form after material creation are unbonded, and thus, are assigned frictional behavior (controlled by parameter ϕ_r). The tensile strengths satisfy a Weibull distribution with mean $\bar{\sigma}_t$ and Weibull modulus m_S , and the cohesion at each contact is correlated with the tensile strength via $c = \gamma\sigma_t$ where γ is the cohesion to tensile strength ratio such that contacts that are stronger/weaker in tension are also stronger/weaker in shear. The shear strength of a subcontact is given by

$$\tau_c = \begin{cases} c + \sigma \tan(\phi), \text{ bonded} \\ \mu F_n, \text{ unbonded with } \mu = \tan\phi_r \end{cases} \tag{4}$$

where ϕ is the friction angle, ϕ_r is the residual friction angle, σ is the normal stress, and F_n is the normal force at the subcontact.

The **grain-strength parameters** assign the following properties to all grains: reference grain size (d_r); Weibull modulus for size effect (m_{SE}); and strength properties of the Hoek-Brown failure criterion with a tension cut-off (σ_c , σ_T , and m_i), with the reference grain tensile strengths satisfying a Weibull distribution with mean $\bar{\sigma}_T^r$ and Weibull modulus m_{SG} , and the UCS correlated with the tensile strength via $\sigma_c = \gamma_g \sigma_T$ where γ_g is the UCS to tensile strength ratio such that grains that are stronger/weaker in tension have a larger/smaller UCS.

1.4 Laboratory Test Modeling Environment

The laboratory test modeling environment supports creation of the SNBV material in the shape of a specimen (cylinder for the 3D model and unit-thickness rectangle for the 2D model) followed by testing of the material in direct tension and compression (triaxial compression for the 3D model and biaxial compression for the 2D model) while tracking and visualizing material damage (with testing properties specified in **`runLabTests.dat`**).

Timestep scaling is activated via the **model mechanical timestep scale** command such that the inertial mass of each particle is scaled such that the stable timestep is 1.0 making the velocity have units of length per step. Kinetic energy can be dissipated via local damping by specifying a non-zero value for the local-damping factor of each grain — quasi-static conditions are modeled by setting the local-damping factor (FISH variable **`localDampFac`**) to 0.7. Dynamic effects can be studied by deactivating timestep scaling and choosing the local-damping factor to correspond with the seismic quality factor of the rock (Potyondy and Cundall, 2004, Eq. 3). The loading platens are walls that move either toward or away from one another at a constant velocity (specified via FISH variable **`platenVel`**). If a quasistatic test is being modeled, then the platen velocity should be set slow enough to insure quasistatic conditions.[11]

Subcontact stiffnesses at the platen-specimen interface are computed by the **compute-stiffness** method with the contact modulus and contact Poisson's ratio equal to the mean contact modulus $\left(\bar{E}_c\right)$ and zero, respectively.[12] For a direct-tension test, the platens are bonded to the material. For a compression test, the friction coefficient of the platen-specimen interface is specified via FISH variable **`platenFric`**.[13] For a confined compression test, the confining stress is applied and maintained as a boundary condition on the specimen sides via the **rblock facet apply stress-normal** command. During the setup phase, the confining stress is applied to the axial boundaries by moving the platens under servo control until the confining stress is obtained. At this stage, the entire specimen boundary is subjected to the confining stress. Before beginning the test, the strains are reset and the servo control is deactivated such that the platens move toward one another at the specified platen velocity.

---

[11] The quasistatic loading rate is the largest platen velocity that gives quasistatic response meaning that reducing the platen velocity below this value does not affect the stress-strain curve — see Potyondy (2025, Section 5.4: Loading Rate). If a specimen is loaded faster than this rate, it will exhibit dynamic effects whereby the peak force will be larger than the quasistatic value. If the synthetic material is heavily damped $(\alpha = 0.7)$, then the quasistatic loading rate of the synthetic material can be much larger than that of a physical test, because the synthetic material does not contain the same dissipative mechanisms as the physical material. A platen velocity of $1\times10^{-10}\ \mathrm{m/step}$ and local-damping factor of 0.7 were used when testing the pink Lac du Bonnet specimens in Potyondy et al. (2025).

[12] {DP: The behavior of this method when applied to a rblock-facet contact should be documented.}

[13] A friction coefficient of 0.02 was used in Potyondy et al. (2025).

Stress and strain for the 3D model are measured as follows

$$\begin{array}{l}\{\sigma_z, \varepsilon_z, \sigma_r, \varepsilon_r\}, \quad \begin{array}{l}\sigma_r = \frac{1}{2}\left(\sigma_x + \sigma_y\right) \\ \varepsilon_r = \sum\left(\dot{\varepsilon}_x + \dot{\varepsilon}_y\right)\Delta t\end{array} \\ \sigma_z \text{ from force on platens} \\ \varepsilon_z \text{ from platen displacements} \\ \sigma_r \text{ average of 3 overlapping measurement spheres along specimen axis} \\ \varepsilon_r \text{ average of 3 overlapping measurement spheres along specimen axis}\end{array} \tag{5}$$

where the z axis is aligned with the cylinder axis (see Figure 11); σ_z and ε_z are the axial stress and strain, respectively; σ_r and ε_r are the radial stress and strain, respectively; $\sigma_i > 0$ is tension and $\varepsilon_i > 0$ is extension; and each measurement sphere (Itasca, 2026)[14] computes an average stress in the spherical region based on the forces acting at all contacts within the region; and (2) an average strain rate $\left(\dot{\varepsilon}_x \text{ and } \dot{\varepsilon}_y\right)$ in the spherical region based on the velocity of the particles within the region.

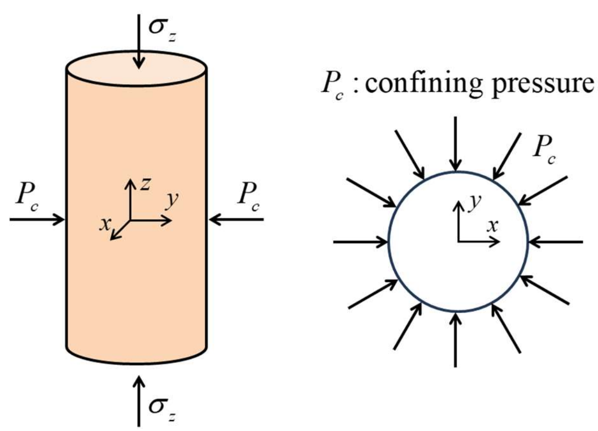

Figure 11 Cylindrical specimen used in a triaxial test showing loading conditions and coordinate system.

[14] In documentation set at PFC: Additional Features: Measure: Measured Quantities.

Stress and strain for the 2D model are measured as follows

$$\begin{array}{l} \{\sigma_y, \varepsilon_y, \sigma_r, \varepsilon_r\}, \quad \begin{array}{c} \sigma_r = \sigma_x \\ \varepsilon_r = \sum \dot{\varepsilon}_x \Delta t \end{array} \\ \sigma_y \text{ from force on platens} \\ \varepsilon_y \text{ from platen displacements} \\ \sigma_r \text{ average of } 3 \text{ overlapping measurement circles along specimen axis} \\ \varepsilon_r \text{ average of } 3 \text{ overlapping measurement circles along specimen axis} \end{array} \tag{6}$$

where the y-axis is aligned with the specimen axis (see Figure 12); σ_y and ε_y are the axial stress and strain, respectively; σ_r and ε_r are the radial stress and strain, respectively; and each measurement circle (Itasca, 2026)[15] computes (1) an average stress in the circular region based on the forces acting at all contacts within the region; and (2) an average strain rate $(\dot{\varepsilon}_x)$ in the circular region based on the velocity of the particles within the region.

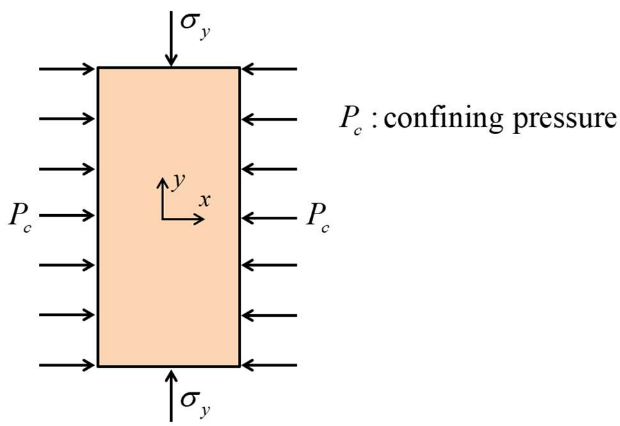

Figure 12 Unit-thickness rectangular specimen used in a confined biaxial test showing loading conditions and coordinate system.

1.4.1 Property Measurement

The following properties are measured during direct-tension and biaxial compression tests: Young's modulus in tension (E_t); direct-tension strength (σ_t); Young's modulus in compression (E_{cc}); Poisson's ratio in compression (ν_{cc}); crack-closure stress (σ_{cc}); crack-initiation stress (σ_{ci}); secondary-cracking stress (σ_{ci2}); crack-damage stress (σ_{cd}); uniaxial compressive strength (σ_{UCS}); and peak differential stress at a confinement of c (σ_{dc}). These properties are extracted from the test results via the file **`getResultsLabTests.dat`**.

[15] In documentation set at PFC: Additional Features: Measure: Measured Quantities.

The tangent Young's modulus and tangent Poisson's ratio are calculated via a moving point regression technique that uses a linear regression fit (see Section 2.2) to a running window of n sampling points (set via FISH variable **`stSize`**)[16] from the stress-strain curve

$$E_{\tan} = \begin{cases} \dfrac{\Delta\sigma_z}{\Delta\varepsilon_z}, & \text{3D model} \\ \dfrac{\Delta\sigma_y}{\Delta\varepsilon_y}, & \text{2D model} \end{cases}, \quad \nu_{\tan} = \begin{cases} -\dfrac{\Delta\varepsilon_r}{\Delta\varepsilon_z}, & \text{3D model} \\ -\dfrac{\Delta\varepsilon_r}{\Delta\varepsilon_y}, & \text{2D model} \end{cases} \tag{7}$$

These expressions are derived in Section 2.3. Line charts of $E_{\tan}$ and $\nu_{\tan}$ versus σ_z are provided in the plots **`slopeTables-compTest`** and **`slopeTables-tenTest`**.

The following properties are measured during a direct-tension test. The Young's modulus in tension (E_t) is taken as the value of $E_{\tan}$ early in the test before any damage has occurred. The direct-tension strength (σ_t) is taken as the maximum value of axial stress.

The following properties are measured during a compression test. The crack-closure stress (σ_{cc}) is taken as the axial stress at which a plot of $E_{\tan}$ versus σ_z becomes constant. The Young's modulus (E_{cc}) and Poisson's ratio (ν_{cc}) in compression are taken as the values of $E_{\tan}$ and $\nu_{\tan}$ at the crack-closure stress (see Figure 13).

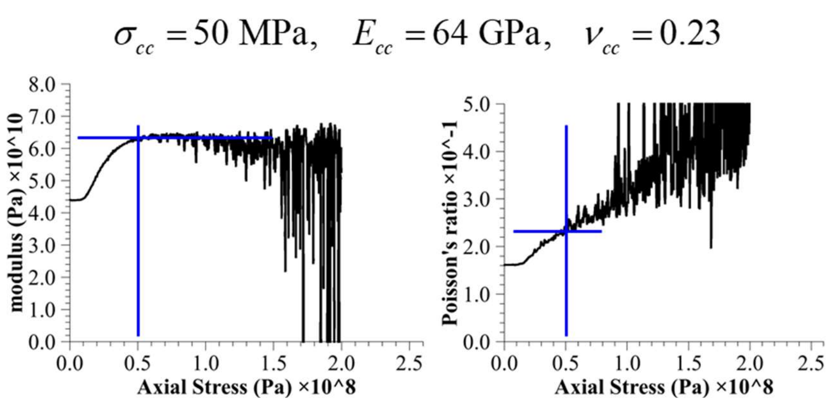

Figure 13 ***Determination of compressive elastic constants and crack-closure stress from UCS test on the large 3D specimen of best-fit material.*** (From Fig. 88 of Potyondy et al. [2024])

The axial stresses at the times of the first interface failure and first broken grain will underestimate the stresses of crack initiation and secondary cracking measured in typical laboratory experiments because the experiments cannot determine these points with such precision. Therefore, the thresholds of crack initiation and secondary cracking are measured as follows. The crack-initiation

[16] A window size of 20 ($n = 20$, **`stSize = 10`**) was used in Potyondy et al. (2025).

stress (σ_{ci}) is taken as the axial stress at the point of crack volumetric strain reversal, where the volumetric (ε_v) and crack volumetric (ε_v^{cr}) strains are computed using the technique described in Martin and Chandler (1994):

$$\varepsilon_v = \begin{cases} \varepsilon_z + 2\varepsilon_r, & \text{3D model} \\ \varepsilon_y + \varepsilon_r, & \text{2D model} \end{cases}, \quad \varepsilon_v^{cr} = \begin{cases} \varepsilon_v - \varepsilon_v^e = \varepsilon_v - \dfrac{1-2\nu}{E}\left(\sigma_z - \sigma_r\right), & \text{3D model} \\ \varepsilon_v - \varepsilon_v^e = \varepsilon_v - \dfrac{1-\nu}{E}\left(\sigma_y - \sigma_r\right), & \text{2D model} \end{cases} \tag{8}$$

The expression for the elastic volumetric strain is derived in Section 2.4. The elastic constants used in this equation should be obtained from the linear portion of the axial stress versus axial strain curve. When plotting crack volumetric strain versus axial strain, ε_v^{cr} is translated downward so that its peak just touches the x axis.[17] The secondary-cracking stress (σ_{ci2}) corresponds with grain breakage; it is taken as the axial stress at which there exists a specified fraction (chosen as 10% in Potyondy et al. [2025]) of the total number of broken grains existing at peak stress. The crack-damage stress (σ_{cd}) is taken as the axial stress at the point of volumetric strain reversal. The peak strength (σ_{UCS}) is taken as the maximum value of axial stress.

1.4.2 Damage Tracking and Visualization

Damage consists of interface and grain breaks.

- **Interface breakage** is tracked and drawn as follows. An interface has three subcontacts (two for the 2D model), each of which can break in tension or shear. A fully broken interface is called a crack; thus, a crack is only created when all subcontacts have broken — partially damaged interfaces are not tracked or drawn. A crack is classified as tensile (all subcontacts have broken in tension), shear (all subcontacts have broken in shear), or mixed. A crack is drawn as a disk (line for the 2D model) with color corresponding to one of the three failure modes, and with area equal to that of the fully broken interface; thus, small cracks are associated with small rigid-block facets. When a grain breaks, the newly created interface and the interfaces on the grain boundary become stress-free, frictional surfaces. The operations on these interfaces are not counted as interface breakage by the crack-tracking scheme.

  The cracks in the **`specimenDamage`** plot are denoted as fractures, and the number of cracks is listed in parentheses following the "Fracture" plot item in the plot legend. Tensile, shear, and mixed cracks are colored red, blue, and black,

[17] The crack volumetric strain is displayed in the plot **`stressStrain_damage-compTest`**. It is computed at the end of the compression test by the FISH function **`crkVolStrain(sa0)`** where **`sa0`** is the axial stress at which to obtain the elastic constants (**`sa0`** must be specified by the user, the default is 0.25 times peak axial stress).

respectively. The number of tensile, shear, and mixed cracks are denoted by n_t, n_s, and n_m, respectively, with FISH variable names of **`niTenBrk, niShBrk, and niMixBrk`**, respectively, and the total number of cracks is denoted by n_c with FISH variable name of **`niBrk`**. A stereonet of crack orientations is provided in the plot **`specimenDamage`**. The stereonet is aligned looking down the specimen axis such that a crack with its normal in the axial direction plots as a point in the center of the stereonet, and a crack aligned parallel with the axis plots as a point on the edge of the stereonet. The crack orientation density is drawn as a color contour. A fracture rosette (radial histogram of crack orientations) is provided for the 2D model. The rosette is aligned looking down the specimen axis such that a crack aligned perpendicular to the axial direction plots at 3:00 o'clock on the rosette.

- **Grain breakage** is tracked and drawn as follows. When a grain breaks, the failure mode is recorded,[18] and the number of mode 1, 2, and 3 breaks are denoted by n_{g1}, n_{g2}, and n_{g3}, respectively, with FISH variable names of **`ng1Brk`**, **`ng2Brk`**, and **`ng3Brk`**, respectively. The total number of breaks is denoted by $n_g = n_{g1} + n_{g2} + n_{g3}$ with FISH variable name of **`ngBrk`**. The grain to be broken is split into two child grains. Each child grain stores the number of times that it has split (by adding one to the number of times that its parent has been split). Each broken grain is drawn as a rigid-block polyhedron and assigned a random color. The number of breakage events is equal to n_g. The number of broken grains is greater than the number of breakage events (see Figure 14). The broken grains and fully broken interfaces are provided in plot **`specimenDamage`**, with coloring of the interface failure modes specified in the "Color Opt" attribute of the "Fracture" plot item. The number of broken grains is listed in parentheses following the "RBlocks" plot item in the plot legend. Line charts[19] of broken interfaces and broken grains versus axial strain for

[18] The failure mode corresponds with the stress state at the time of failure as shown in Fig. 22 of Potyondy et al. (2025).
[19] Line charts (xy pairs joined by lines) are provided by the History Chart and Table Chart plot items.

direct-tension and compression tests are provided in plots **stressStrain_damage-{ten,comp}Test**.

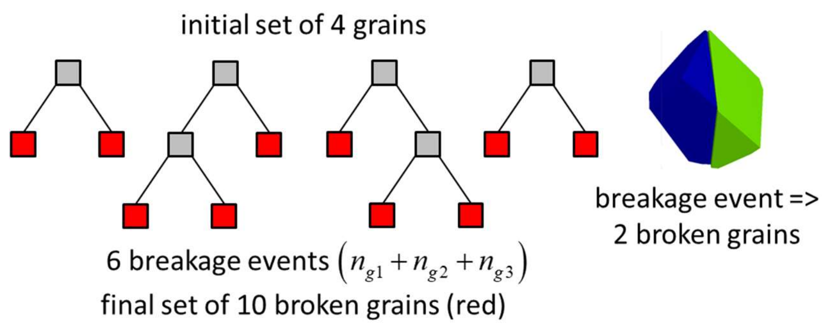

Figure 14 Grain-breakage process and typical broken grain.

1.4.3 Plots

The title bar at the top of each plot contains the material name (FISH variable **matName** specified in file **makeMaterial.dat**) and specimen resolution (defined in Eq. (2)). The line-chart labels assume that the model uses SI units (e.g., stress is labelled as having units of Pascals). The probability density histograms require the specification of the number of bins in the file **makeMaterial.dat**.

The following plots are provided. The figures show results for the models described in Section 0.

- **specimen** The specimen is shown with each grain colored by its ID (which is a unique positive integer) to allow one to differentiate the grains (see Figures 15 and 16).
- **propGrains** Grain-size distribution, probability density histogram of grain tensile strength, and grain-strength (mean) envelope are provided (see Figures 17 and 18181818).
- **propContacts** Probability density histograms of interface tensile strength, contact modulus, and microcrack fabric gap as well as cumulative distribution function of microcrack fabric gaps and slits are provided (see Figures 19 and 20).
- **specimenDamage** The specimen is shown along with broken interfaces and broken grains as well as displacement field and contact force chains. A line chart of axial stress versus axial strain and a stereonet of crack orientations are also provided (see Figures 21–24).
- **stressStrain_damage-tenTest** Line charts of broken interfaces, broken grains, and axial stress versus axial strain for a direct-tension test are provided (see Figures 25 and 26).
- **stressStrain_damage-compTest** Line charts of broken interfaces, broken grains, axial stress, volumetric strain, and crack volumetric strain versus axial strain

for a compression test are provided (see Figures 27 and 28). A line chart of axial stress versus radial strain is also provided in the plot-item list but not shown. The volumetric-strain line chart is created after the test is complete.

- **`slopeTables-{ten,comp}Test`** Line charts of tangent Young's modulus $(E_{\tan})$, tangent Poisson's ratio $(\nu_{\tan})$, tangent lateral stiffness $(\Delta\sigma_z/\Delta\varepsilon_r)$, and tangent volumetric stiffness $(\Delta\sigma_z/\Delta\varepsilon_v)$ versus axial stress for a direct-tension and compression test are provided (see Figures 29–32). These line charts are created after the test is complete.

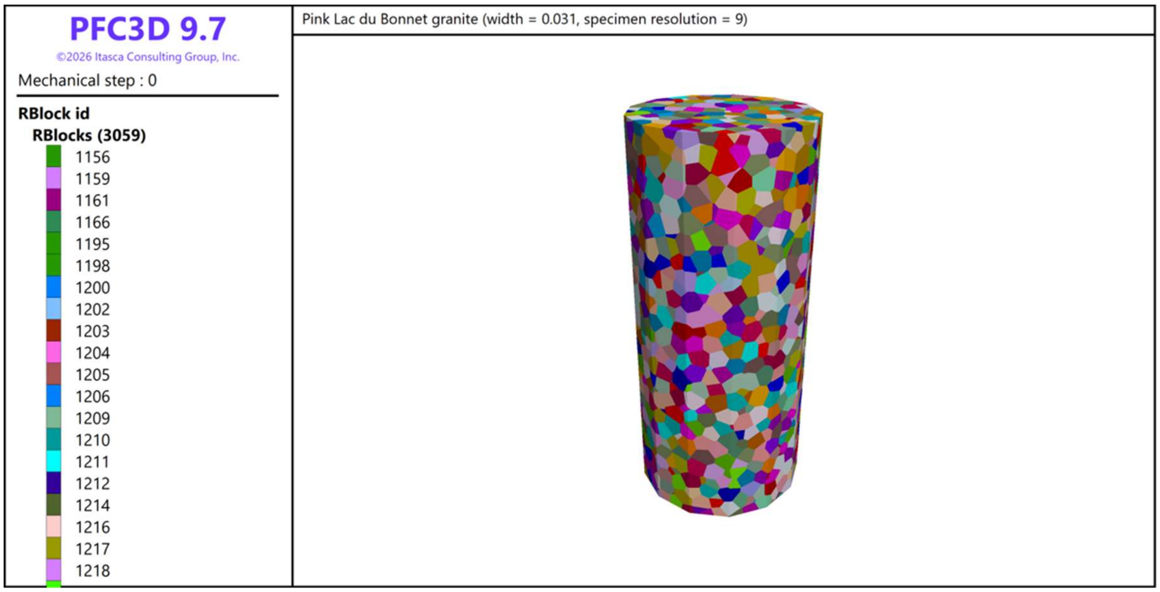

Figure 15 ***PFC3D plot*** **`specimen`.**

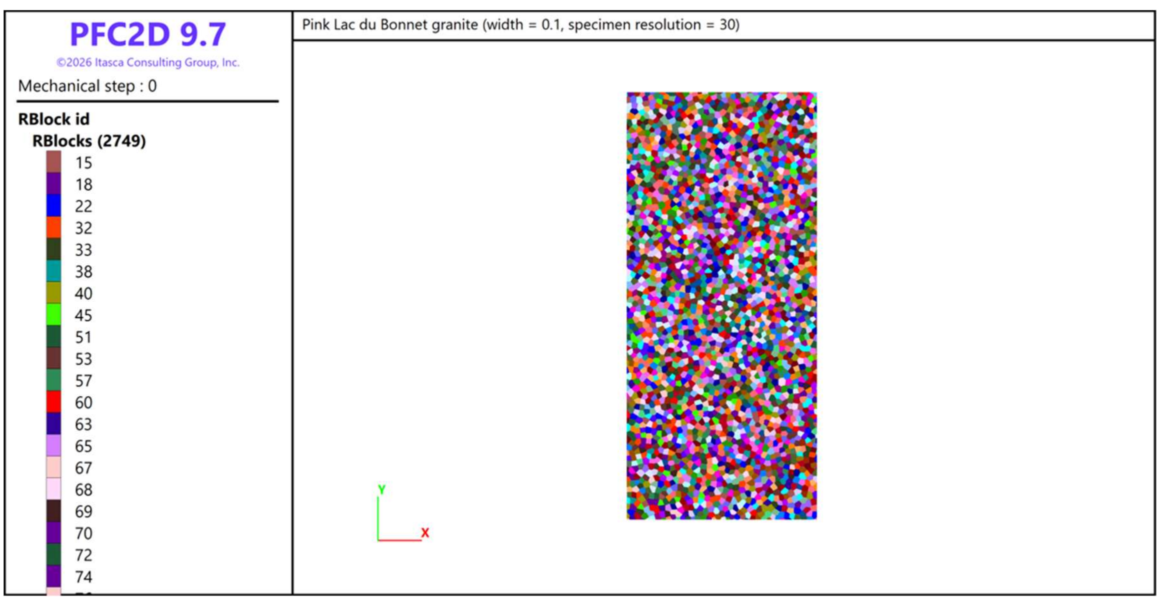

Figure 16 ***PFC2D plot*** **`specimen`.**

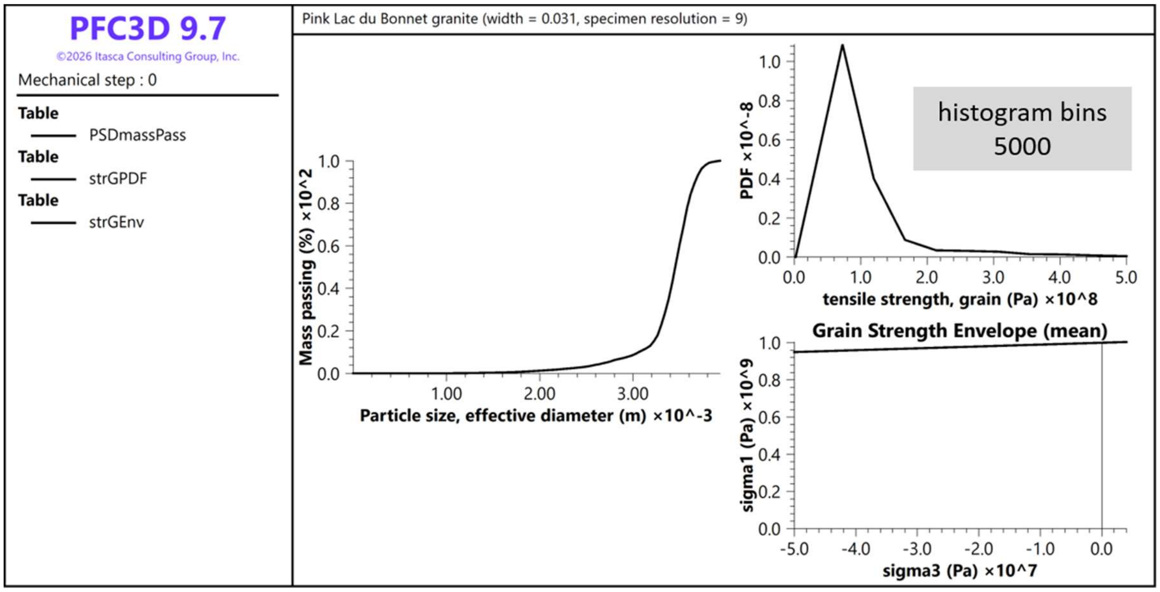

Figure 17 ***PFC3D plot*** **`propGrains`.**

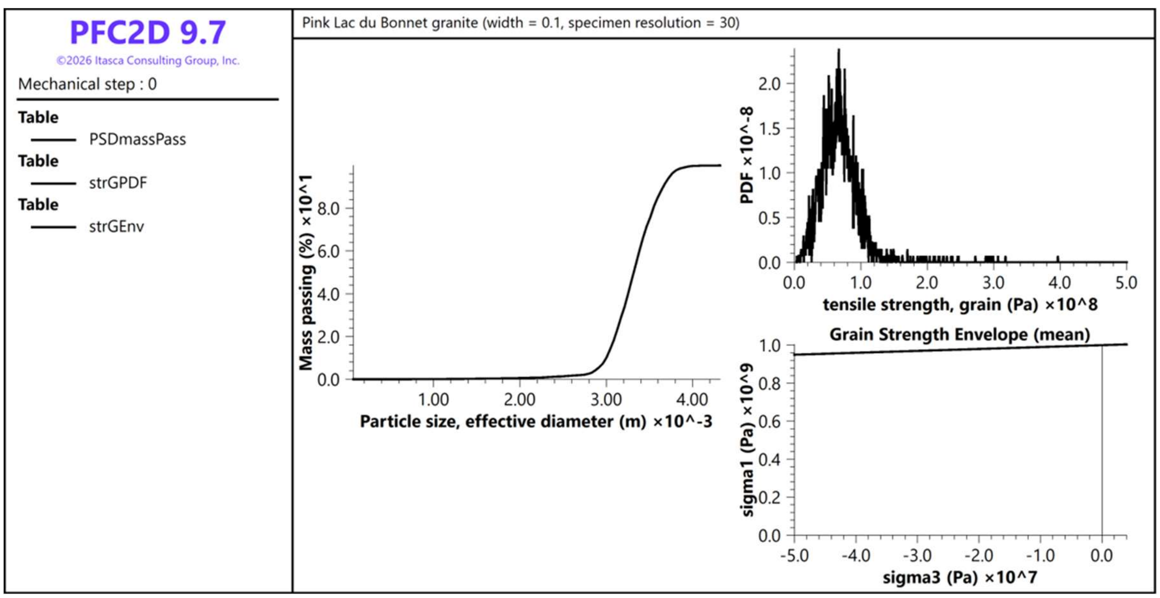

Figure 18 ***PFC2D plot*** **`propGrains`.**

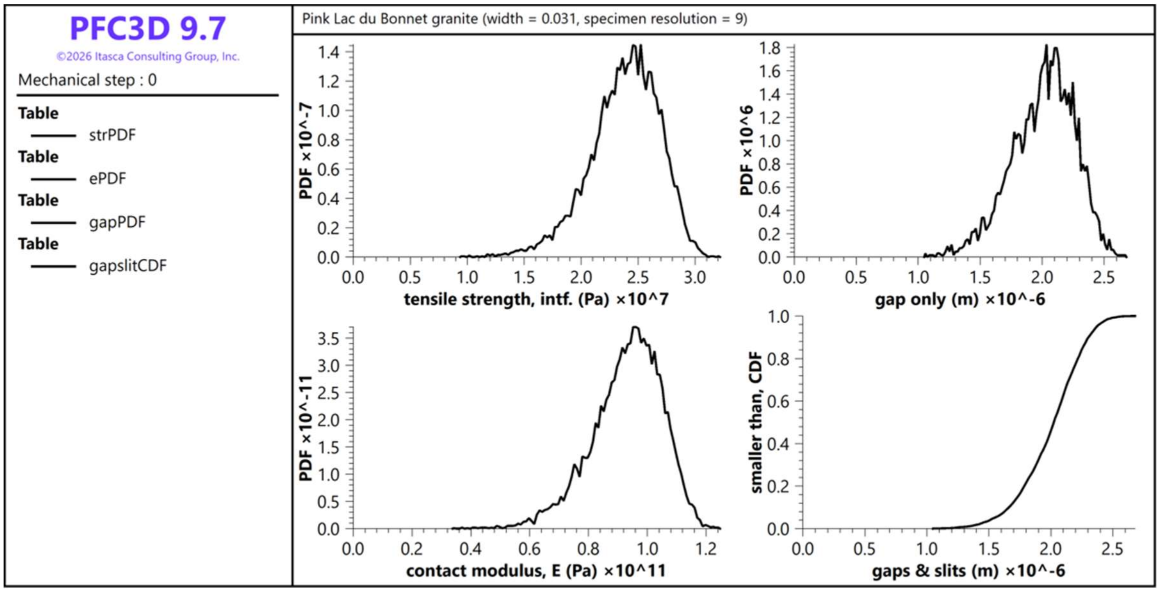

Figure 19 ***PFC3D plot*** **`propContacts`.**

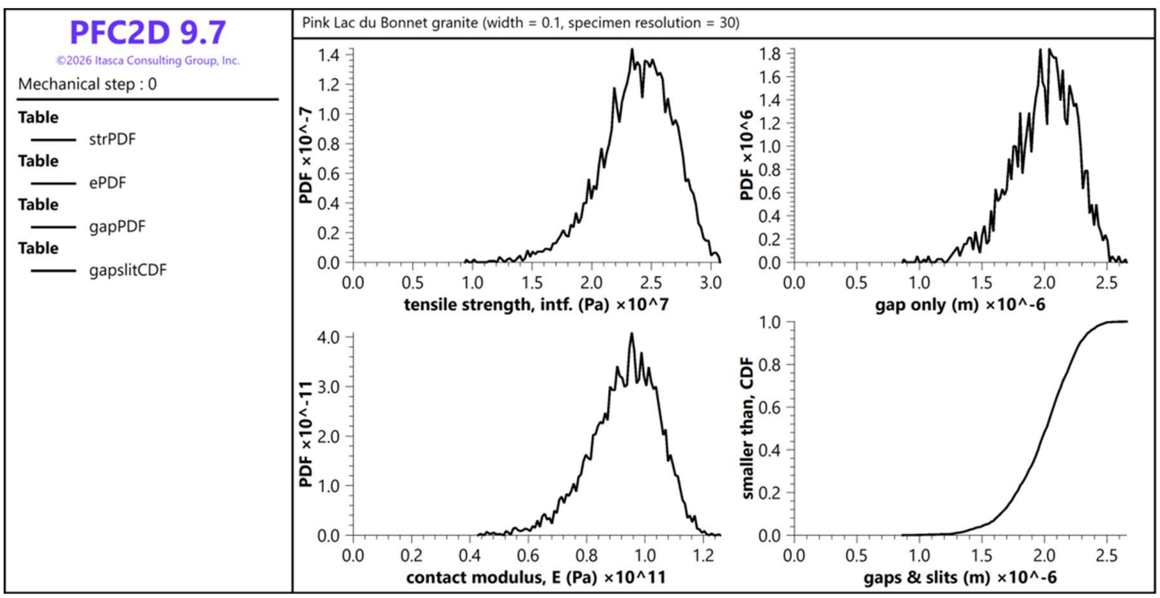

Figure 20 ***PFC2D plot*** **`propContacts`.**

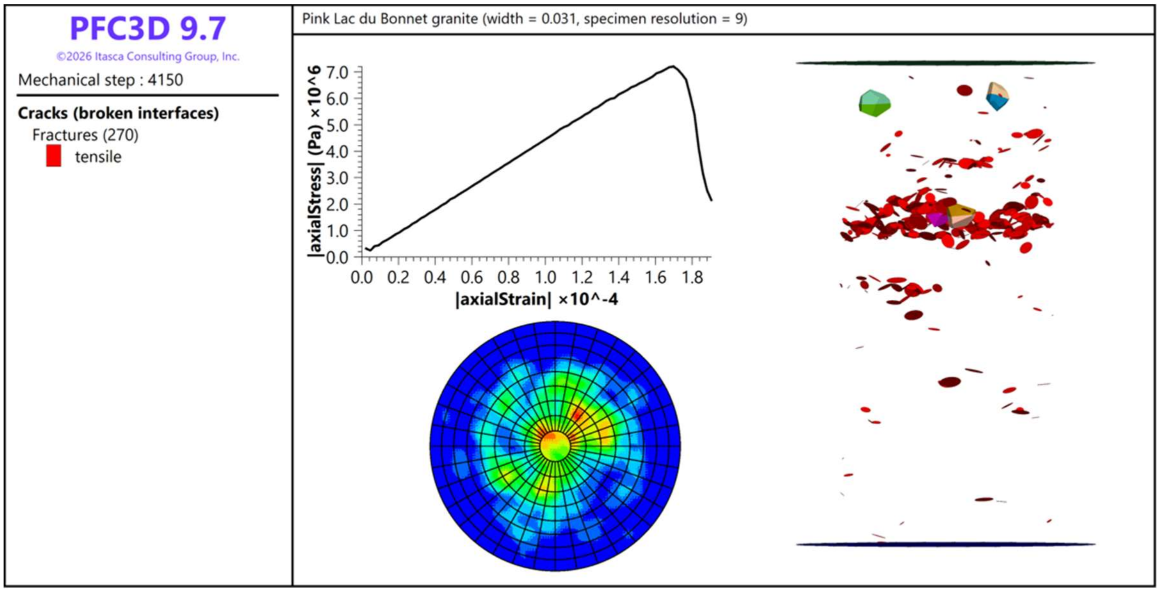

Figure 21 ***PFC3D plot*** **`specimenDamage`** ***at end of direct-tension test.***

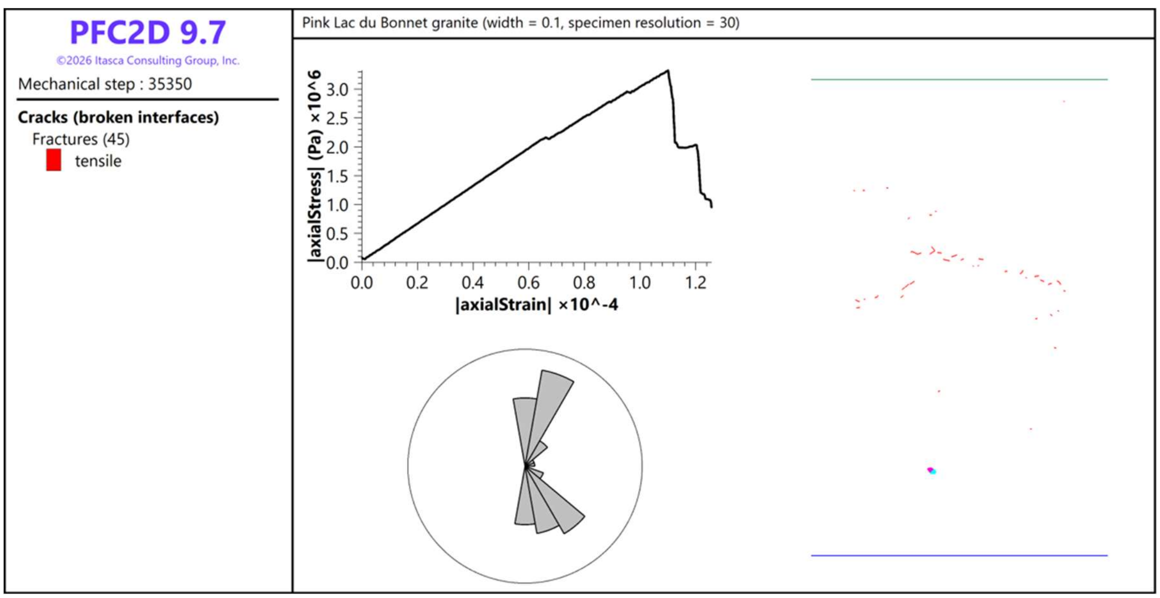

Figure 22 ***PFC2D plot*** **`specimenDamage`** ***at end of direct-tension test.***

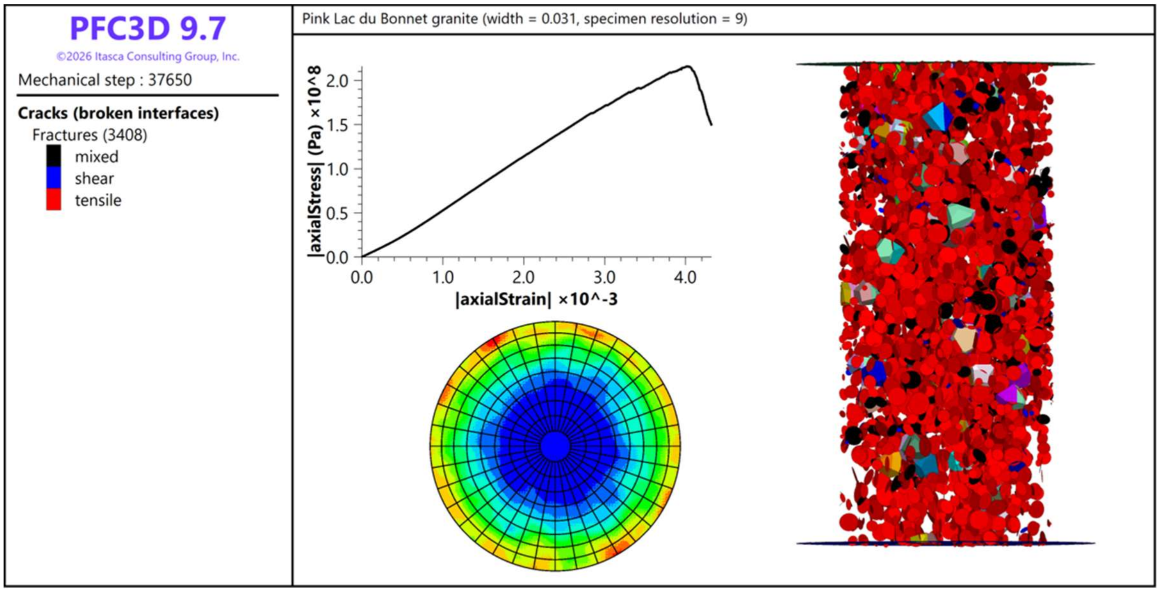

Figure 23 ***PFC3D plot*** `specimenDamage` ***at end of UCS test.***

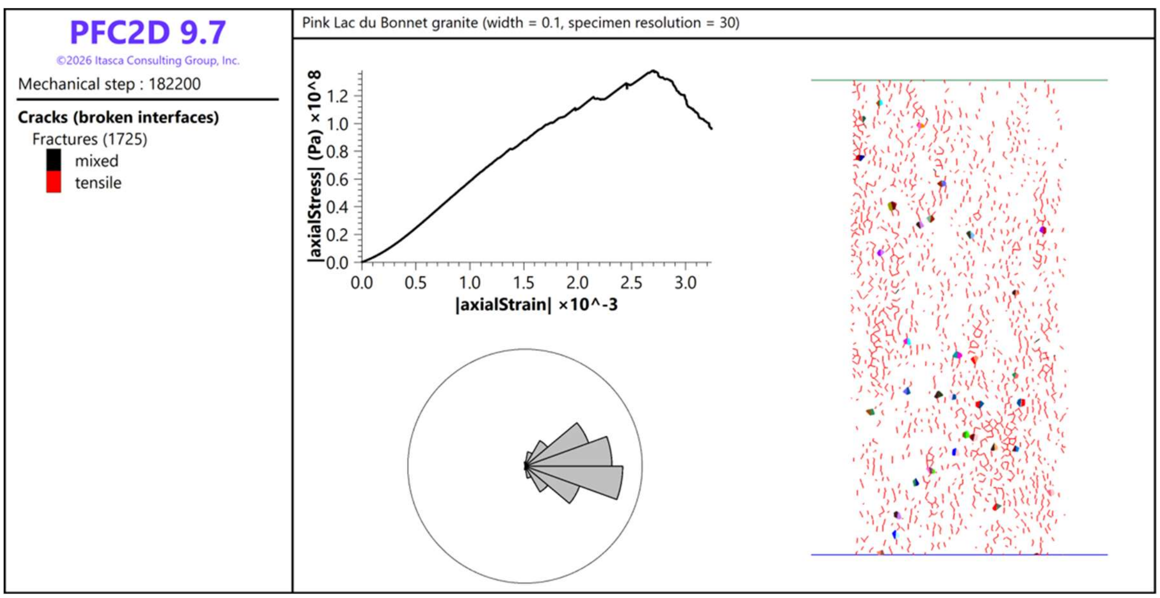

Figure 24 ***PFC2D plot*** `specimenDamage` ***at end of UCS test.***

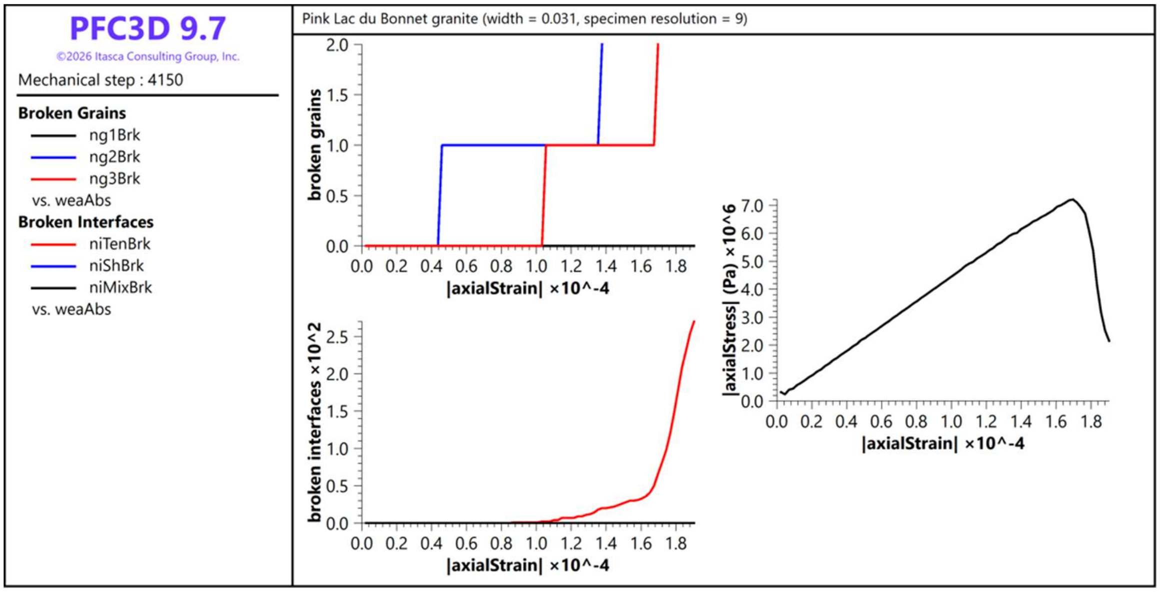

Figure 25 ***PFC3D plot*** `stressStrain_damage-tenTest` ***at end of direct-tension test.***

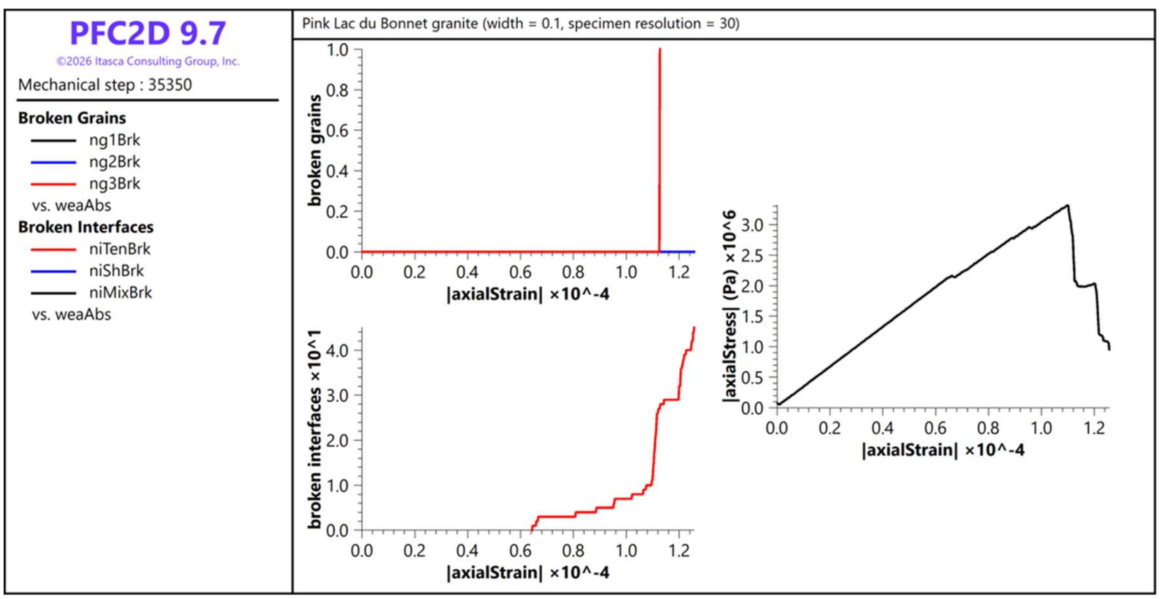

Figure 26 ***PFC2D plot*** `stressStrain_damage-tenTest` ***at end of direct-tension test.***

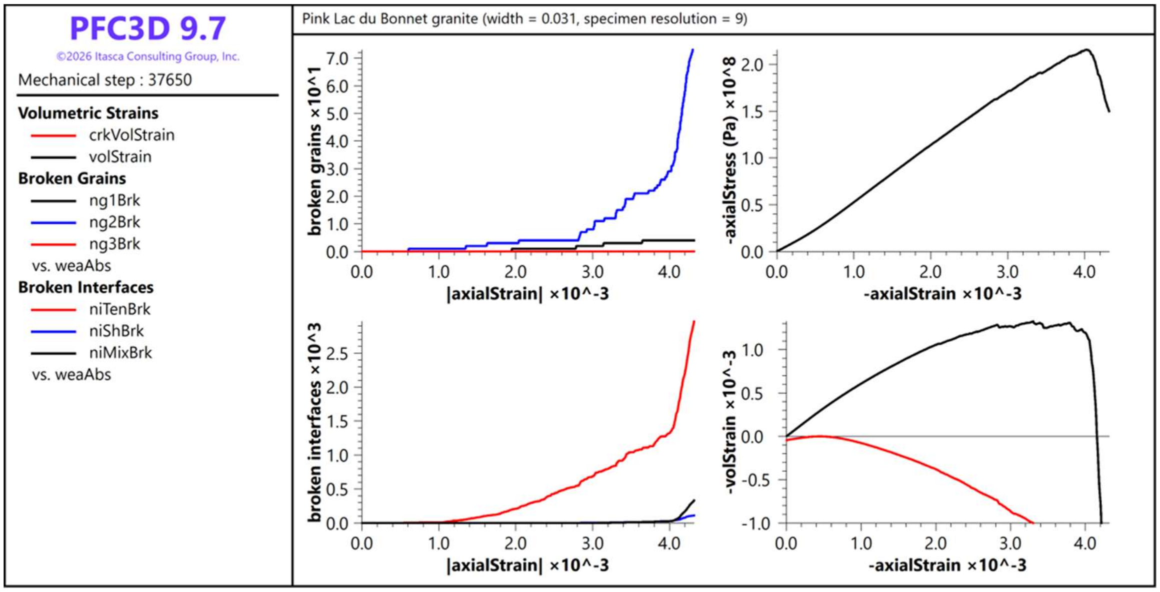

Figure 27 ***PFC3D plot*** `stressStrain_damage-compTest` ***at end of UCS test.***

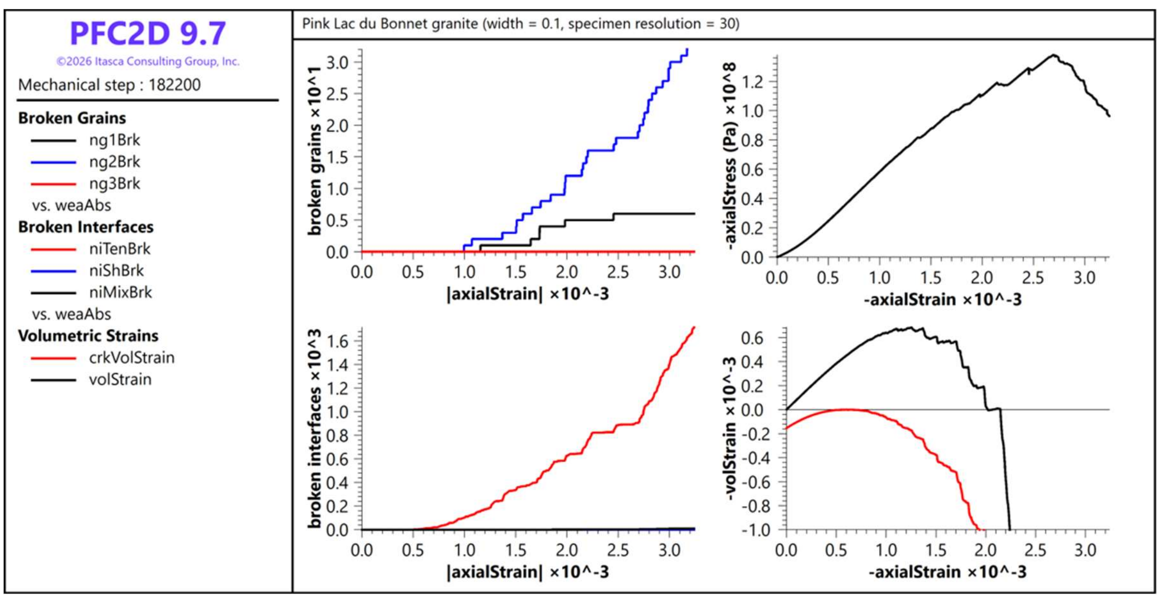

Figure 28 ***PFC2D plot*** `stressStrain_damage-compTest` ***at end of UCS test.***

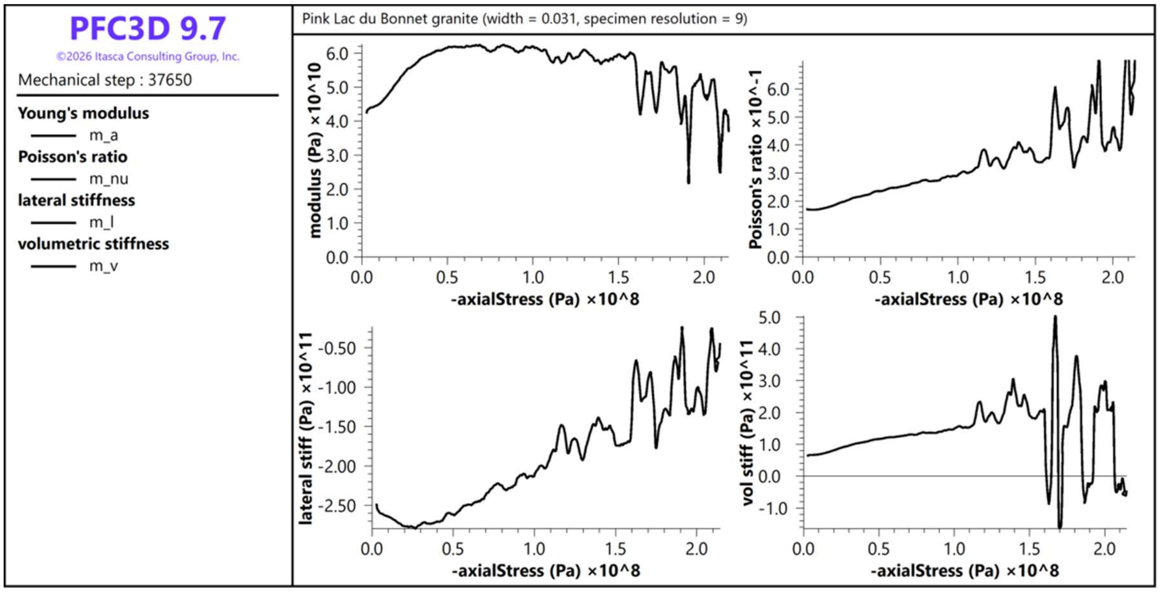

Figure 29** PFC3D plot* `slopeTables-compTest` ***at end of UCS test.

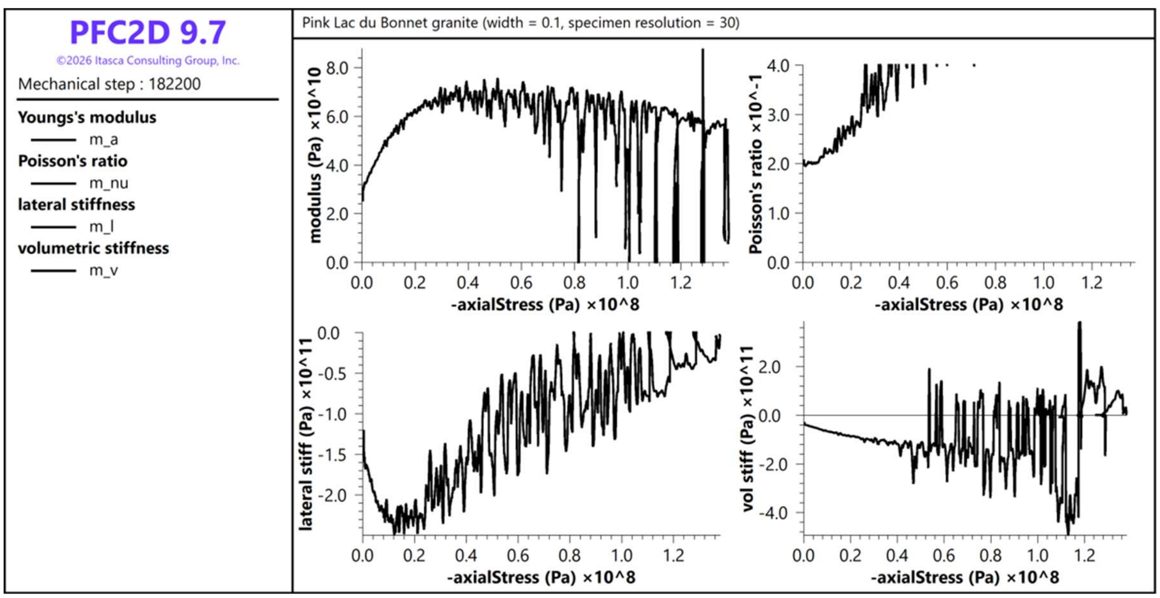

Figure 30** PFC2D plot* `slopeTables-compTest` ***at end of UCS test.

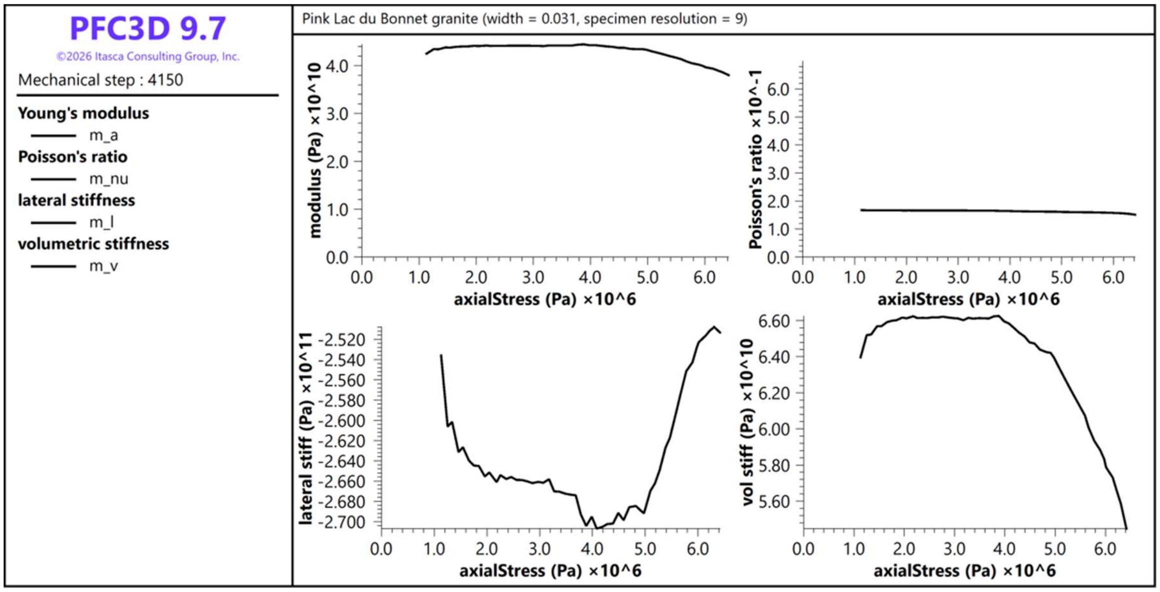

***Figure 31** PFC3D plot `slopeTables-tenTest` at end of direct-tension test.*

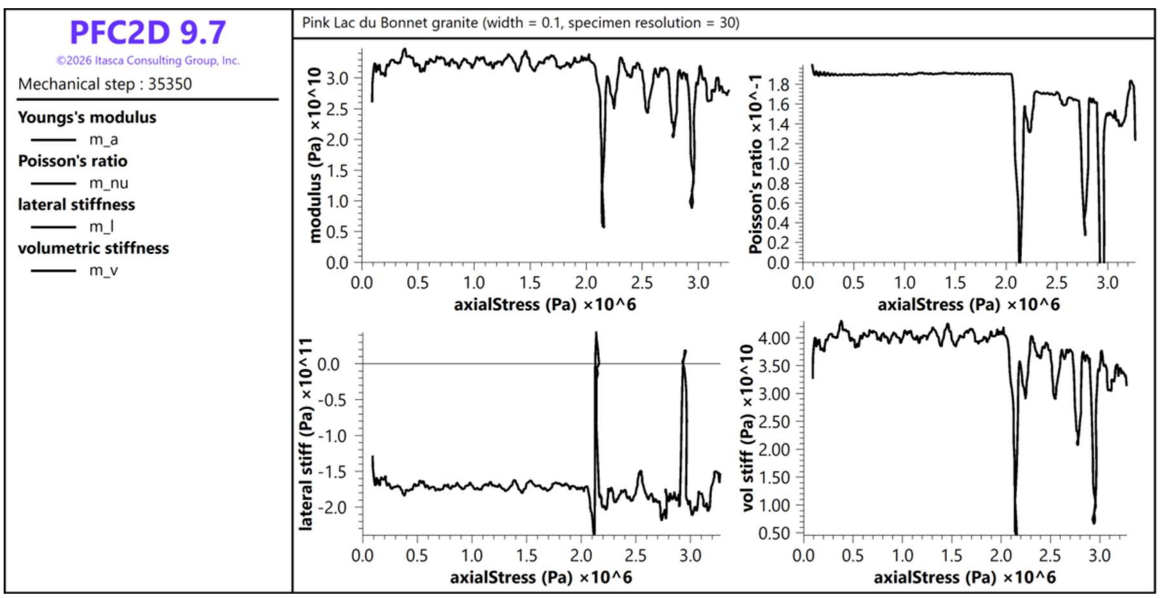

***Figure 32** PFC2D plot `slopeTables-tenTest` at end of direct-tension test.*

1.5 Example Material

The version number of the SNBV package is in **`ExampleProjects3D\snbvSrc\snbvPkg-VERSION.txt`**. The test suite is launched by opening the project **`LabTests3D.p3prj`** in the directory **`ExampleProjects3D\LabTests3D`** and calling the data file **`doAll.dvr`**.[20] The small

[20] The corresponding files for PFC2D replace the threes with twos — e.g., **`ExampleProjects2D`**. The file-naming conventions are given in **`snbvPkg-README`**.txt. The loading rate for the models described here is just above the upper limit of being quasistatic such that the peak stresses may be a few percent higher and

specimen of the best fit material for pink Lac du Bonnet granite from Potyondy et al. (2025) is created and tested (see Figure 33). The microproperties of this material are listed in Table 2.

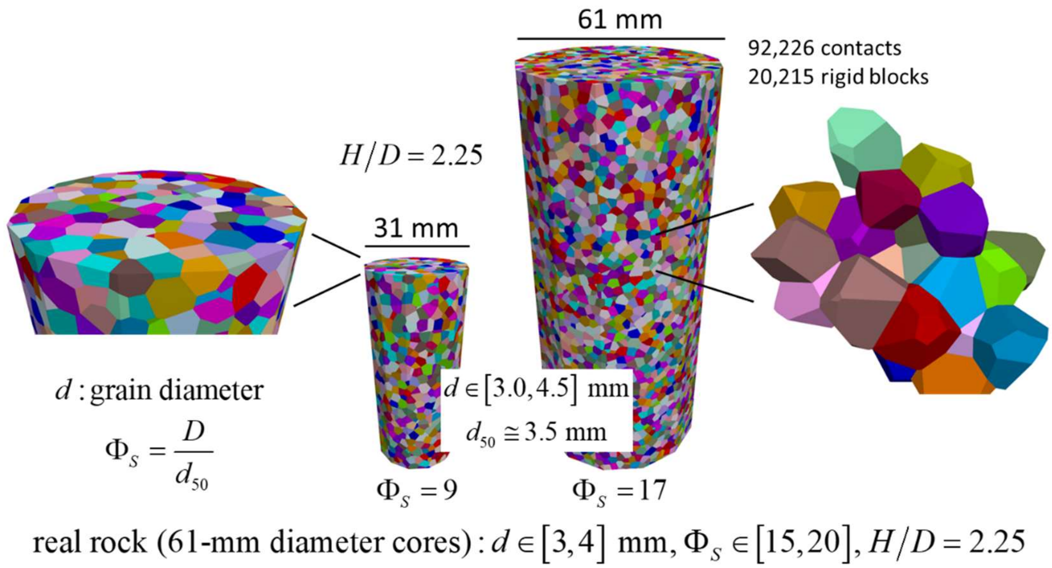

Figure 33 Synthetic and real rock specimens. (From Fig. 28 of Potyondy et al. [2025])

the post-peak stress-strain curves may exhibit a less abrupt stress drop than their quasistatic values. The current loading rate should be sufficient for purposes of model development and calibration. The final models should be rerun at a reduced loading rate that is quasistatic.

Table 2 Microproperties* of Pink Lac du Bonnet Granite Material

Deformability

$\bar{E}_c$ (GPa)	m_E	ν_c
93	9.4	0.25

Microcrack Fabric

φ_B	φ_G	$\bar{g}$ (μm)	m_G
0.7	0.3	2	9.4

Interface Strength

$\bar{\sigma}_t$ (MPa)	m_S	γ	ϕ (deg)	ϕ_r (deg)
23.8	9.4	13.6	20	20

Grain Strength

d_r (mm)	$\bar{\sigma}_T^r$ (MPa)	m_{SG}	γ_g	m_i	m_{SE}
4.8	50	3.0	20	0.01	3.0

* Parameters are defined in Table 1.

2.0 APPENDICES

2.1 Weibull Distribution

The Weibull distribution is a continuous probability distribution that can fit an extensive range of distribution shapes. The Weibull distribution is used to introduce material heterogeneity into the SNBV material (via the deformability, microcrack fabric, and strength properties) and to characterize the size effect on grain strength. The Weibull distribution is described in this subsection, which begins with a brief review of probability theory taken from Lindgren et al. (1978).

The **probability density function** of random variable X is denoted by $f_X(x)$ and is defined such that $P(a < X < b) = \int_a^b f(x)\,dx$ with properties:

$$f(x) \ge 0, \quad \int_{-\infty}^{\infty} f(x)\,dx = 1 \tag{9}$$

The **cumulative distribution function** of random variable X is defined as $F_X(x) = P(X \le x)$, for all $x \in \mathbb{R}$ with properties

$$0 \le F(x) \le 1, \quad F'(x) \ge 0, \quad F(-\infty) = 0, \quad F(\infty) = 1 \tag{10}$$

If X is attributed to the individuals of a population, then $F(x)$ may be defined as the number of individuals having an $X \le x$, divided by the total number of individuals.

The **mean value** or expected value of random variable X is defined as

$$\mu \equiv E(X) \equiv \int_{-\infty}^{\infty} x\, f(x)\,dx \tag{11}$$

The **standard deviation** of random variable X is defined as

$$\sigma_X = \sqrt{\operatorname{var} X} = \sqrt{E(X^2) - \left[E(X)\right]^2}, \quad \text{var is variance} \tag{12}$$

The following material is from "Weibull distribution" (2024). The **Weibull probability density function** is defined as

$$f_W(x; m, x_o) = \begin{cases} \dfrac{m}{x_o}\left(\dfrac{x}{x_o}\right)^{m-1} e^{-(x/x_o)^m}, & x \ge 0 \\ 0, & x < 0 \end{cases} \tag{13}$$

where $x_o > 0$ is characteristic value (or scale parameter) with

$$F_W(x_o) = 1 - e^{-1} \cong 0.632$$

$m > 0$ is shape factor (or shape parameter) [-]

The general form of f_W has an additional parameter called the threshold parameter (x_u), which gives the minimum value in the distribution. The SNBV material properties that satisfy a Weibull distribution are all positive; thus, we set $x_u = 0$ to obtain Eq (13).

The **Weibull cumulative distribution function** is defined as

$$F_W(x;m,x_o) = \begin{cases} 1 - e^{-(x/x_o)^m}, & x \geq 0 \\ 0, & x < 0 \end{cases} \tag{14}$$

The **mean value of the Weibull distribution** is defined as

$$\mu_W = x_o \, \Gamma\left(1 + \frac{1}{m}\right) \tag{15}$$

where Γ is the gamma function: $\Gamma(z) = \int_0^\infty e^{-x} x^{z-1} dx$. The **standard deviation of the Weibull distribution** is defined as

$$\sigma_W = x_o \left[\Gamma\left(1 + \frac{2}{m}\right) - \Gamma^2\left(1 + \frac{1}{m}\right) \right]^{1/2} \tag{16}$$

The function f_W in Eq. (13) is expressed in terms of a characteristic value and shape factor. The SNBV material properties that satisfy a Weibull distribution are expressed in terms of a mean value and shape factor by rearranging Eq. (15) to obtain

$$x_o = \mu_W \Big/ \Gamma\left(1 + \frac{1}{m}\right) \tag{17}$$

The Weibull distribution can be characterized in terms of a uniform distribution as follows ("Weibull distribution," 2024). If U is uniformly distributed on $(0,1)$, then the random variable

$$W = x_o \left[-\ln(U) \right]^{1/m} \tag{18}$$

is Weibull distributed with parameters x_o and m. A Weibull distribution is assigned to a model property using Eq. (18). The effect of the mean and shape factor on the probability density and cumulative distribution functions are illustrated in Figure 34. The dispersion decreases as the shape factor increases and the mean is not at the peak of the probability density.

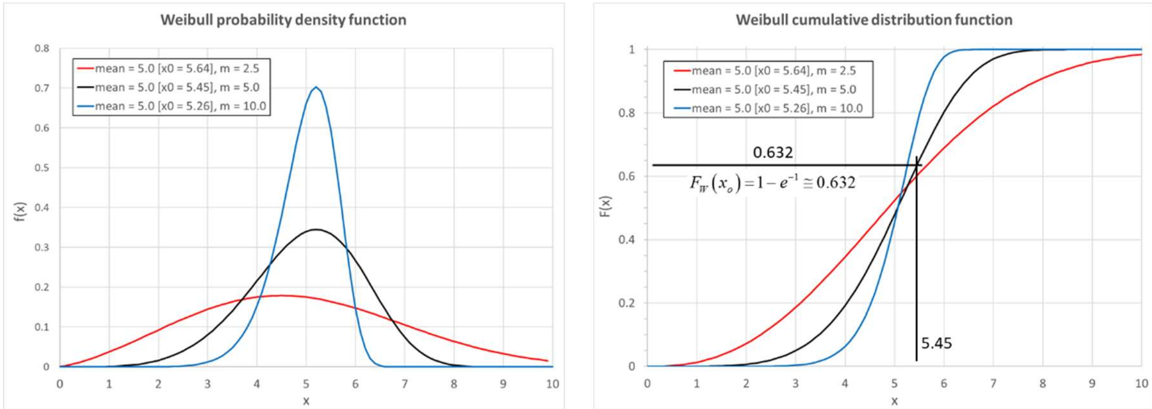

Figure 34 Effect of mean and shape factor on the Weibull probability density and cumulative distribution functions.

2.2 Best-fit Line

The best-fit line is a linear regression model with the ordinary least-squares method such that the line minimizes the sum of squared residuals (differences between actual and predicted values of the dependent variable y_i). Given a set of n data pairs $\{(x_i, y_i), i = 1, \ldots, n\}$, the line that provides a best fit to these data pairs is given by ("Simple linear regression," 2025)

$$y = \alpha + \beta x$$

$$\alpha = \frac{\sum_{i=1}^{n} y_i \sum_{i=1}^{n} x_i^2 - \sum_{i=1}^{n} x_i \sum_{i=1}^{n} x_i y_i}{n \sum_{i=1}^{n} x_i^2 - \left(\sum_{i=1}^{n} x_i \right)^2} \tag{19}$$

$$\beta = \frac{n \sum_{i=1}^{n} x_i y_i - \sum_{i=1}^{n} x_i \sum_{i=1}^{n} y_i}{n \sum_{i=1}^{n} x_i^2 - \left(\sum_{i=1}^{n} x_i \right)^2}$$

where α and β are the y-intercept and slope, respectively, of the line (see Figure 35).

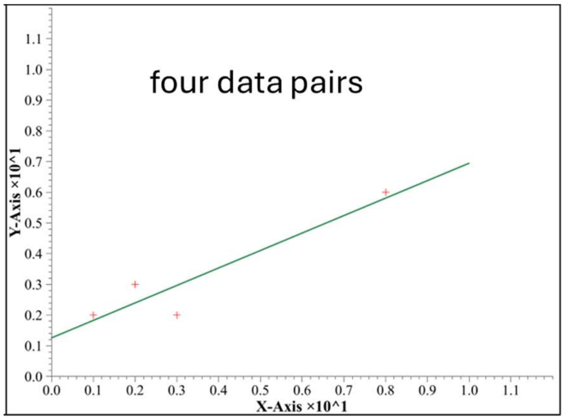

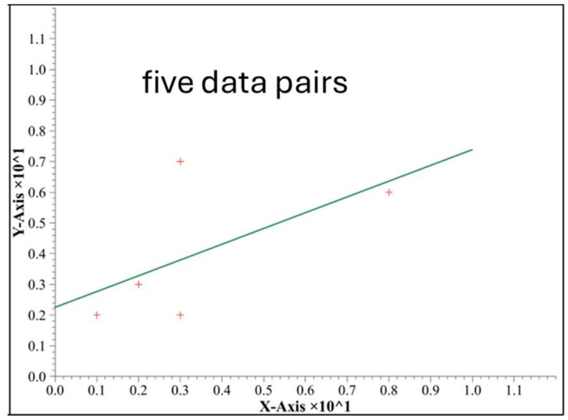

Figure 35 Best-fit lines for sets of four and five data pairs.

2.3 Measuring Elastic Constants

Expressions for the elastic constants measured during triaxial (in 3D) and biaxial (in 2D) tests are derived in this appendix. The measurement assumes that the specimen behaves as a linear elastic isotropic body.

2.3.1 Triaxial Test

The constitutive relations for a linear elastic isotropic material are

$$\begin{aligned} \varepsilon_x &= \frac{1}{E}\left[\sigma_x - \nu\left(\sigma_y + \sigma_z\right)\right] \\ \varepsilon_y &= \frac{1}{E}\left[\sigma_y - \nu\left(\sigma_x + \sigma_z\right)\right] \\ \varepsilon_z &= \frac{1}{E}\left[\sigma_z - \nu\left(\sigma_x + \sigma_y\right)\right] \end{aligned} \qquad \begin{aligned} \gamma_{xy} &= \tau_{xy}/G \\ \gamma_{xz} &= \tau_{xz}/G, \quad G = \frac{E}{2(1+\nu)} \\ \gamma_{yz} &= \tau_{yz}/G \end{aligned} \tag{20}$$

where the elastic constants are Young's modulus (E) and Poisson's ratio (ν).

The elastic constants can be measured by performing a triaxial test as shown in Figure 11. The loading conditions are as follows

$$\begin{aligned} \text{initial conditions:} &\quad \sigma_x = \sigma_y = \sigma_z = P_c \\ \text{during test:} &\quad \begin{cases} \sigma_x = \sigma_y = P_c \ (\text{constant}) \\ \sigma_z \ \text{varies} \end{cases} \end{aligned} \tag{21}$$

where P_c is the confining pressure. We obtain expressions for the elastic constants by substituting the increments of stress and strain that occur during the test after confinement application into the incremental form of Eq. (20):

$$\begin{gathered}\Delta\sigma_x = \Delta\sigma_y = \Delta\gamma_{xy} = \Delta\gamma_{xz} = \Delta\gamma_{yz} = 0 \\ \Delta\sigma_z \neq 0\end{gathered} \tag{22}$$

$$\Delta\varepsilon_x = \frac{-\nu}{E}\Delta\sigma_z \tag{23}$$

$$\Delta\varepsilon_y = \frac{-\nu}{E}\Delta\sigma_z \tag{24}$$

$$\Delta\varepsilon_z = \frac{1}{E}\Delta\sigma_z \tag{25}$$

The Young's modulus is obtained from Eq. (25) as

$$E = \frac{\Delta\sigma_z}{\Delta\varepsilon_z} \tag{26}$$

The Poisson's ratio is obtained by substituting Eq. (26) in Eq. (24), and solving for ν:

$$\nu = -\frac{\Delta\varepsilon_y}{\Delta\varepsilon_z} \tag{27}$$

We define the radial strain

$$\varepsilon_r = \varepsilon_x = \varepsilon_y \tag{28}$$

such that the expression for the Poisson's ratio becomes

$$\nu = -\frac{\Delta\varepsilon_r}{\Delta\varepsilon_z} \tag{29}$$

The tangent Young's modulus and tangent Poisson's ratio defined in Eq. (7) correspond with the expressions of Eqs. (26) and (29), respectively.

2.3.2 Biaxial Test

The constitutive relations for a linear elastic isotropic material are given by Eq. (20) where the elastic constants are Young's modulus (E) and Poisson's ratio (ν). The constitutive relations for a 2D DEM linear elastic isotropic material (consisting of rigid unit-thickness particles):

$$\begin{aligned}\varepsilon_x &= \frac{1}{E'}\left[\sigma_x - \nu'\sigma_y\right] \\ \varepsilon_y &= \frac{1}{E'}\left[\sigma_y - \nu'\sigma_x\right]\end{aligned} \qquad \gamma_{xy} = \tau_{xy}/G', \quad G' = \frac{E'}{2(1+\nu')} \tag{30}$$

where E' and ν' are the effective Young's modulus and effective Poisson's ratio, respectively. The relations in this equation are obtained by noting that there is no stress or strain in the out-of-plane direction (the unit-thickness particles are rigid and do not expand or contract), and thus, we remove σ_z and ε_z from the 3D constitutive relations of Eq. (20), and disregard the third equation for ε_z. This is the constitutive relation for a linear elastic isotropic material subjected to plane-stress boundary conditions $\left(\sigma_z = \tau_{xz} = \tau_{yz} = 0\right)$. It would be interesting to determine whether a 2D bonded material, perhaps of a thin plate with a circular hole loaded in uniaxial tension with plane-stress boundary conditions, would match this analytical solution. The question to answer is: Does the 2D DEM material (with no frictional sliding and before bond breakage) behave as a linear elastic isotropic body subjected to plane stress boundary conditions.

The values of E' and ν' can be measured by performing a biaxial test as shown in Figure 12. The loading conditions are as follows

$$\begin{gathered}\text{initial conditions: } \sigma_x = \sigma_y = P_c \\ \text{during test: } \begin{cases} \sigma_x = P_c \ \left(\text{constant}\right) \\ \sigma_y \ \text{varies} \end{cases}\end{gathered} \tag{31}$$

where P_c is the confining pressure. We obtain expressions for the effective elastic constants by substituting the increments of stress and strain that occur during the test after confinement application into the incremental form of Eq. (30):

$$\begin{gathered}\Delta\sigma_x = \Delta\gamma_{xy} = 0 \\ \Delta\sigma_y \neq 0\end{gathered} \tag{32}$$

$$\Delta\varepsilon_x = \frac{-\nu'}{E'}\Delta\sigma_y \tag{33}$$

$$\Delta\varepsilon_y = \frac{1}{E'}\Delta\sigma_y \tag{34}$$

The effective Young's modulus is obtained from Eq. (34) as

$$E' = \frac{\Delta\sigma_y}{\Delta\varepsilon_y} \tag{35}$$

The effective Poisson's ratio is obtained by substituting Eq. (35) into Eq. (33), and solving for ν':

$$\nu' = -\frac{\Delta\varepsilon_x}{\Delta\varepsilon_y} \tag{36}$$

We define the radial strain

$$\varepsilon_r = \varepsilon_x \tag{37}$$

such that the expression for effective Poisson's ratio becomes

$$\nu' = -\frac{\Delta\varepsilon_r}{\Delta\varepsilon_y} \tag{38}$$

The tangent Young's modulus and tangent Poisson's ratio defined in Eq. (7) correspond with the expressions of Eqs. (35) and (38), respectively.

2.4 Measuring Elastic Volumetric Strain

Expressions for the elastic volumetric strain measured during triaxial (in 3D) and biaxial (in 2D) tests are derived here.

2.4.1 Triaxial Test

The elastic volumetric strain that occurs during a triaxial test is derived here. This is the volumetric strain that occurs after confinement application as the applied axial stress increases. The relevant stress-strain relations are given by Eqs. (21) to (25). The volumetric strain that occurs during the test after confinement application is given by

$$\varepsilon_v^e = \varepsilon_x + \varepsilon_y + \varepsilon_z = \frac{1-2\nu}{E}\left(\sigma_z - P_c\right), \quad \sigma_z > P_c \tag{39}$$

The elastic volumetric strain defined in Eq. (8) is found by noting that the confining stress is equal to the radial stress:

$$\varepsilon_v^e = \frac{1-2\nu}{E}\left(\sigma_z - \sigma_r\right), \quad \sigma_z > \sigma_r \tag{40}$$

2.4.2 Biaxial Test

The elastic volumetric strain that occurs during a biaxial test is derived here. This is the volumetric strain that occurs after confinement application as the applied axial stress increases. The relevant stress-strain relations are given by Eqs. (31) to (34). The volumetric strain that occurs during the test after confinement application is given by

$$\varepsilon_v^e = \varepsilon_x + \varepsilon_y = \frac{1-\nu}{E}\left(\sigma_y - P_c\right), \quad \sigma_y > P_c \tag{41}$$

The elastic volumetric strain defined in Eq. (8) is found by noting that the confining stress is equal to the radial stress:

$$\varepsilon_v^e = \frac{1-\nu}{E}\left(\sigma_y - \sigma_r\right), \quad \sigma_y > \sigma_r \tag{42}$$

3.0 REFERENCES

Asahina, D., Aoyagi, K., Kim, K., Birkholzer, J. T., & Bolander, J. E. (2017). Elastically-homogeneous lattice models of damage in geomaterials. *Computers and Geotechnics, 81*, 195–206. https://doi.org/10.1016/j.compgeo.2016.08.015

Asahina, D., Ito, K., Houseworth, J. E., Birkholzer, J. T., & Bolander, J. E. (2015). Simulating the Poisson effect in lattice models of elastic continua. *Computers and Geotechnics, 70*, 60–67. https://doi.org/10.1016/j.compgeo.2015.07.013

Bolander, J. E., & Sato, S. (1998). Fracture analyses using spring networks with random geometry. *Engineering Fracture Mechanics*, *61*, 569–591. https://doi.org/10.1016/S0013-7944(98)00069-1

ITASCA. (2026). PFC Suite — Particle Flow Code in Two and Three Dimensions (Version 9.0). Itasca Consulting Group, Inc. https://www.itascainternational.com/software/pfc

Lindgren, B. W., McElrath, G. W., & Berry, D. A. (1978). *Introduction to Probability and Statistics* (4th ed.). Macmillan Publishing Company.

Martin, C. D., Chandler, N. A. (1994). The progressive fracture of Lac du Bonnet granite. *Int. J. Rock Mech. & Min. Sci.*, *31*(6), 643–659. https://doi.org/10.1016/0148-9062(94)90005-1

Oreskes, N., Shrader-Frechette, K., & Belitz, K. (1994). Verification, validation, and confirmation of numerical models in the earth sciences. *Science*, *263*, 641–646. https://doi.org/10.1126/science.263.5147.641

Potyondy, D. (2025). Material-modeling support for PFC [fistPkg9.3]. Itasca Consulting Group, Inc., Technical Memorandum ICG7766-L (April 24, 2025). https://www.itascacg.com/software/material-modeling-support

Potyondy, D. O. (2015). The bonded-particle model as a tool for rock mechanics research and application: current trends and future directions. *Geosystem Engineering, 18*(1), 1–28. https://doi.org/10.1080/12269328.2014.998346

Potyondy, D. O., & Cundall, P. A. (2004). A bonded-particle model for rock. *Int. J. Rock Mech. & Min. Sci.*, *41*(8), 1329–1364. https://doi.org/10.1016/j.ijrmms.2004.09.011

Potyondy, D. O., Fu, W., Purvance, M., & Mas Ivars, D. (2025). A 3D subspring network breakable voronoi model for rock. *Rock Mechanics and Rock Engineering*, https://doi.org/10.1007/s00603-025-04655-w.

Potyondy, D. O., & Purvance, M. (2024). A 3D subspring network breakable voronoi model for rock: grain-breakage scheme. In *Applied Numerical Modeling in Geomechanics 2024* (*Proceedings, Sixth International Itasca Symposium, June 2024)* (J. Hazzard, M. Nelson, T. Katsaga, & J.

Sanftenberg, Eds.), Paper 04-10. ISBN 978-0-9767577-6-4. Itasca International, Minneapolis. https://www.itascacg.com/events/6th-itasca-symposium-on-applied-numerical-modeling

Potyondy, D. O., & Fu, W. (2024). A 3D subspring network breakable voronoi model for rock: laboratory-scale behavior. In *Proceedings of the 58th US Rock Mechanics/Geomechanics Symposium*, Paper ARMA 24-493. American Rock Mechanics Association. https://doi.org/10.56952/ARMA-2024-0493

Potyondy, D., Fu, W., & Emam, S. (2024). Micromechanical spalling model: subspring network breakable voronoi material. Itasca Consulting Group, Inc., Report to Svensk Kärnbränslehantering AB (SKB), Stockholm, Sweden, 2-5732-03:23R57, February 23, 2024.

Rasmussen, L. L. (2026). Email message to David Potyondy, May 21, 2026.

Rasmussen, L. L. (2021). Hybrid lattice/discrete element method for bonded block modeling of rocks. *Computers and Geotechnics*, *130*, 103907. https://doi.org/10.1016/j.compgeo.2020.103907

Rasmussen, L. L. (2022). A breakable grain-based model for bi-modular rocks. *Int. J. Rock Mech. & Min. Sci.*, *151*, 105028. https://doi.org/10.1016/j.ijrmms.2021.105028

Simple linear regression. (2025, January 17). In *Wikipedia*. https://en.wikipedia.org/wiki/Simple_linear_regression

Weibull distribution. (2024, December 2). In *Wikipedia*. https://en.wikipedia.org/wiki/Weibull_distribution

Winsberg, E. (2010). *Science in the age of computer simulation*. University of Chicago Press.